Chemosphere 355 (2024) 141751

Contents lists available at ScienceDirect

Chemosphere

journal homepage: www.elsevier.com/locate/chemosphere

Prediction and optimizing of methylene blue sequestration to activated charcoal/magnetic nanocomposites using artificial neutral network and response surface methodology

Uyiosa Osagie Aigbe [a,*], Thabang Calvin Lebepe [b], Oluwatobi Samuel Oluwafemi [b,c], Otolorin Adelaja Osibote [a]

[a] Department of Mathematics and Physics, Faculty of Applied Sciences, Cape Peninsula University of Technology, Cape Town, South Africa

[b] Department of Chemical Sciences (Formerly Applied Chemistry), University of Johannesburg, Doornfontein Campus, Johannesburg, South Africa

[c] Centre for Nanomaterials Science Research, University of Johannesburg, P. O. Box 17011, Doornfontein, 2028, Johannesburg, South Africa

HIGHLIGHTS

- An optimal sorption capacity of 455 mg g^{-1} was established from this study.
- The PSOM and FRHM adequately define MB confiscation to AC/Fe_3O_4 NCs.
- The quadratic model with an R^2 value of 0.9857 perfectly explained the sorption process of MB dye.
- The LM best predict the sorption of MB to AC/Fe_3O_4 NCs with an R^2 value of 0.9922.

GRAPHICAL ABSTRACT

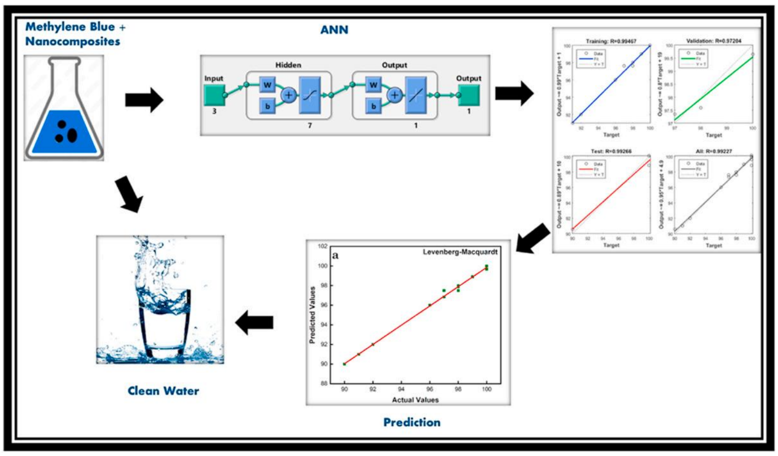

ARTICLE INFO

Handling Editor: Jun Huang

Keywords:
Nanoparticles
Nanocomposites
ANN
RSM
Isotherm
Kinetic

ABSTRACT

Green synthesized magnetic nanoparticles (MNPs) linked with activated charcoal (AC) (AC/Fe_3O_4 NCs) were exploited for methylene blue (MB) confiscation in this study. The AC/Fe_3O_4 NCs produced were characterized using TEM, FTIR, UV/Vis and XRD spectrometry. The Response-Surface-Methodology (RSM) was utilized to improve the experimental data for the MB sorption to AC/Fe_3O_4 NCs, with 20 experimental runs implemented through a central composite design (CCD) to assess the effect of sorption factors-initial MB concentration, pH and sorbent dosage effects on the response (removal-effectiveness). The quadratic model was discovered to ideally describe the sorption process, with an R^2 value of 0.9857. The theoretical prediction of the experimental data using the Artificial-Neural-Network (ANN) model showed that the Levenberg-Marquardt (LM) had a better performance criterion. Comparison between the modelled experimental and predicted data showed also that the

* Corresponding author.
E-mail address: uyi4we@gmail.com (U.O. Aigbe).

https://doi.org/10.1016/j.chemosphere.2024.141751
Received 25 September 2023; Received in revised form 18 January 2024; Accepted 16 March 2024
Available online 22 March 2024

LM algorithm had a high R^2 of 0.9922, which showed NN model applicability for defining the sorption of MB to AC/Fe_3O_4 NCs with practical precision. The results of the non-linear fitting (NLF) of both isotherm and kinetic models, showed that the sorption of MB to AC/Fe_3O_4 NCs was perfectly described using the pseudo-second-order (PSOM) and Freundlich (FRHM) models. The estimated optimum sorption capacity was 455 mg g^{-1}. Thermodynamically, the sorption of MB to AC/Fe_3O_4 NCs was shown to be non-spontaneous and endothermic.

1. Introduction

In recent years, intense global threats have been enhanced from air contamination, worldwide warming and more prominently, the contamination of drinking water sources (Martis et al., 2022). In the human world, colour plays a critical role. In the current state of affairs, around 10,000 or more dyes are accessible commercially and approximately 7 million tons of dyes yearly are manufactured globally (Dey and Dey, 2021; Aigbe et al., 2021; Yang et al., 2022; Richard et al., 2022). In various industrial processes, natural dyes are generally used in leather dyeing, textiles, wood, paper, plastics, silk, cosmetics, pharmaceutical and food productions. Industrial waste from textile, paper, printing, leather, cosmetics, and food production is most often released into water bodies. Presently, contamination by synthetic dyes in the above-catalogued productions is getting huge interest around the globe due to their adverse effects on public health and the marine biota (Richard et al., 2022; Makhado et al., 2022; Aigbe et al., 2018; Eleryan et al., 2023).

Through colour permeation of the receiving water and the subsequent inhibition of sunlight from entering the water are enhanced by dye wastewater released into the marine ecosystem, so marine life is destroyed (Ramutshatsha-Makhwedzha et al., 2022). In addition, almost all dyes are particularly toxic and cancer-causing and have mutagenic and teratogenic impacts on marine and human life at very minimal concentrations. With tinctorial values of 1 mg.L^{-1}, cationic dyes have been described to be extra noxious than anionic dyes (Ghoniem et al., 2022).

One of the most utilized dyes for industrial processes especially in fabric manufacturing is MB (chemical formula-$C_{16}H_{18}C_1N_3S$), employed for fabric dyeing and finishing. However, considerable contact with MB is dangerous to humans and marine life as it can cause vomiting, skin sensitivities, limb paralysis, sensory system issues, shock, tissue death, impacts on the reproductive system, renal damage, cancer, and cardiovascular destruction. Owing to these adverse effects ascribed to MB complexity, stability and aromatic structure, MB is challenging to degrade under normal circumstances, hence, MB confiscation from industrial discharges has attracted worldwide interest (Ramutshatsha-Makhwedzha et al., 2022; Zheng et al., 2018; Archana et al., 2022; Buhani et al., 2023a; Eldeeb et al., 2022).

Diverse methods employed to remediate MB effluents are membrane separation/filtration, ion-exchange, electrochemical process, precipitation, flocculation, photocatalytic degradation, etc. Nevertheless, these procedures are not cost-efficient, are required to conform with a sequence of regulations and are not presented on the marketplace for small-scale effluent treatment activities. Taking all these into consideration and the increasing importance of the green industry, water-based sorption remediation has appeared as a general preference over other technologies, and it is greatly dependent on the sorbent characteristics like the distribution of surface charge, the ratio of surface area-to-volume and porosity. Sorption has been reported to be effective in terms of its effortless design and straightforward procedure both in batch and continuous process, elevated effectiveness, low-cost and callousness to noxious materials and low-cost sorbent materials accessibility (Zheng et al., 2018; Razali et al., 2020; Xia et al., 2019; Al-Zawahreh et al., 2021; Abussaud et al., 2016). One of the most important factors in the sorption process' effectiveness is choosing the appropriate sorbent, one that is compatible with the adsorbate being adsorbed in terms of both type and nature. The anticipated sorbent needs to be chemically stable, reusable, have a high sorption rate and capacity, and be eco-friendly (Buhani et al., 2023b).

Lately, there has been an intensified consideration for the utilization of naturally derived materials with various formations and innovative structures such as activated charcoal (AC) and NPs synthesized with plant extracts support to create NCs for the effective dye molecules sorption (Al-Zawahreh et al., 2021; Martis et al., 2022; Igwegbe et al., 2019). Carbon-recognized sorbent materials, which are non-polar and hydrophobic, have good potential for contaminants sequestration from industrial effluents owing to their extraordinary surface-area, a well-created porosity and the tunable-surface comprising of functional-groups which improve their sorption efficacy (Abussaud et al., 2016; Aigbe et al., 2023a).

In recent years, environmental substances have been utilized progressively as sorbents for this process owing to their low cost and straightforward alteration (KAYA and ERDEM, 2023). Activated charcoal (AC) has demonstrated excellent sorption performance for a comprehensive collection of contaminants owing to its permeable structure, extraordinary reactivity surface and extraordinary individual surface area. However, the use of AC on a substantial scale in various sectors is constrained by the hurdle of separating it from water-soluble solutions, secondary contamination creation and cost-ineffective non--recyclability. To overcome this issue, AC-based magnetic NCs powder has attracted much attention and is effectively applied in dye molecule removal owing to the ease of controlling and swiftly separating them from the solution through external field applications (Nistor et al., 2021; Moosavi et al., 2020; Abdel-Ghani et al., 2019; Juang et al., 2018).

Magnetic particles as sorbents have created a new area in separation technology among the many kinds of sorbents. Depending on the industrial effluent attributes, magnetic separation can be a capable remediation approach with a straightforward and swift recovery. It is crucial for the dispersal of particles following waste sorption. Magnetic sorbent application can improve the cross-linking and thermal stability of the sorbents. This approach can enhance the time and effectiveness of urban treatment plants. This approach links the physicochemical phase of sorption and a magnetic filtration phase (Moosavi et al., 2020; Elwakeel et al., 2016). Notwithstanding metal oxides such as Fe_3O_4 nanoparticles (NPs) morphological attributes like controlled size, superior surface area and extraordinary reactive sites, there has been a greater requisite for non-toxic, eco-friendly magnetic NPs with production capability using the green synthesis approach employing extracts from plants (Aigbe et al., 2023b). The plant bio-molecules present in the extract of the plant have the possibility of stabilizing and reducing metal salts into NPs to avoid aggregation of the NPs (Vinayagam et al., 2021, 2022; Geneti et al., 2022; Parajuli et al., 2020; Nguyen et al., 2022). Inserting MNPs in other materials gives an extra reactive centre and improves the surface area. These materials have been recognized as effective sorbents with small diffusion resistance (Elwakeel et al., 2020).

Currently, NPs biosynthesis employing extracts of plant leaves has attracted huge attention from researchers owing to extracts of plant leaves containing flavonoids which are water-soluble metabolites of plants with reducing and stabilizing capabilities for efficient NPs fabrication. These flavonoids have a hydroxyl (OH) group, which is transformed from the enol structure to the keto structure, thereby creating a reactive hydrogen atom that decreases the metallic-ions into NPs. These plants' bio-molecules allow for the reduction and stabilization/capping of NPs to discourage aggregation (Mfon et al., 2020).

Fe_3O_4 NPs were bio-produced using leaf extract from the Ocimum

Fig. 1. Image of OG leaf.

Gratissimum (OG) plant in this study. OG also identified as scent-leaf is a communal spice belonging to the Lamiaceae plant family and is also acknowledged as African-basil/clover basil/Ntoong (Fig. 1). It is an aromatic enduring herb plant which is prevalent in West Africa, India, Mexico, Bolivia, Southern Asia, Brazil and the Caribbean. It is mostly grown in Indonesia to extract oil and its leaves are utilized as a tea. From the available literature, it has been mostly employed for diseases such as headache, haemorrhoids, inflammation, pneumonia, and convulsion treatment, for keeping wounds sterilized and improving the effectiveness of antibiotics. Also, extracts of OG leaf have generally been utilized in certain metal inhibition, antimicrobial activity and noxiousness assessment (Mfon et al., 2020; Eddy et al., 2022; Ikimi and Abosede, 2022; Prabu et al., 2017; Onyebuchi and Kavaz, 2019; Bankole et al., 2020; Narendra Kumar et al., 2019; Solomon et al., 2019; Sharma et al., 2020).

These processes are initiated via metallic substance nucleation and hence NPs outgrowth begins from anywhere it is created as a precipitate inside the mixture. Additionally, the natural material discovered in microorganisms and plants plays a part in the stabilization/capping of NPs as they bind to the nanostructure surface, thereby inhibiting particle agglomeration and nullifying the demand for extra stabilizing agents (Drummer et al., 2021).

In most sorption process experimental designs, one factor at a time (OFAT) is used. This technique aims to assess the influence of specific factors on the process being investigated. The approach is easy to use but has drawbacks. It assumes that the factors under study are discrete and their impacts on the process are linear and additive. But in most cases, these factors are discrete, and their influence is NL and interactive. Hence, OFAT, may not capture the actual process nature and recognize the ideal settings for the efficient removal of contaminants. Therefore, a more broad and methodical techniques like RSM and ANN models are needed to optimize and predict the sorption process of MB dye to AC/Fe_3O_4 NCs (Banza et al., 2023a; Simbi et al., 2022).

The RSM is a combination of numerical approaches that is efficient for creating, improving and optimizing processes, in which many discrete input variables influence the dependent output variables (response), unlike the OFAT. It is an improved methodical technique of experimentation, as it assesses all system variables instantaneously while predicting an outcome. RS statistics involves a whole factorial design created on a multi-nominal NL prototype whereby all variables vary through diverse acknowledged tests. A key plus of this model is that it requires reduced experimental runs to establish the optimum experimental setting (Banza et al., 2023a; Natrayan et al., 2024)

Soft computing approaches like ANN, genetic algorithms (GA), fuzzy logic (FL)-based approaches (fuzzy inference systems-FIS), and various connectionist systems (Adapted Neuro-Fuzzy Inference System-ANFIS) are progressively documented as precise learning systems for modelling multifaceted phenomena in various engineering, physical, and natural science domains. These approaches can address the uncertainties that regularly build up in more conventional mathematical and statistical approaches (Agbaogun et al., 2023). As a widespread unconventional modelling approach among the modernisation computing procedures, the ANN method has been used effectively to model NL associations involved in multifaceted chemical procedures like adsorption. This approach does not need an extra typical experimental design for model building (Amor et al., 2021). In solid–liquid sorption systems, ANNs are broadly utilized to estimate the rate of sorption of an adsorbent. based on the available experimental information, the network output is determined by the ANN. It also suggests approximating numerical functions for both linear and NL systems. The model is trained to predict the sorption output which is well-thought-out to be the equilibrium concentration of the solute in the solution. (Ararem et al., 2014).

A novel simplistic NCs were produced by blending AC with MNPs created using OG leaf extract under ultrasound wave irradiation (>20 kHz) in this study (Yildiz, 2018). Hence, this research's fundamental objective is to develop low-cost and eco-friendly NCs under ultrasound wave irradiation and generate a machine-learning model for the sorption process prediction based on the ANN model as well as apply a mathematical and statistical approach like the RSM model to experimental designs, statistical study and modelling and numerical optimization of the sorption of MB to AC/Fe_3O_4 NCs based on input variables (pH, initial MB concentration and sorbent dosage). The % of MB removed was also predicted via ANN from the generated RSM data set and the results were linked with experimental values. The predictive ability of the NN was assessed to create an optimum by the selection of parameters which were assessed using R^2, MSE and RMSE values in this study.

2. Materials and methods

In this study, analytical chemical grades were utilized without added purification. Sodium chloride (NaOH), hydrochloric-acid (HCl), sodium chloride (NaCl), MB, ferrous sulphate ($FeSO_4.7H_2O$), ferric chloride ($FeCl_3.6H_2O$), and AC were bought from Merck, South Africa. A concentrated solution of (1000 $mg.L^{-1}$) MB was produced by weighing 1 g of the dye into a litre volumetric-flask and dissolving it using deionized water (DW). Afterwards, the required dye concentrations were produced from the Concentrated solution of MB.

2.1. OG leaf extract preparation

OG leaf extract was prepared according to the method by (Aigbe et al., 2023b). The OG leaves were obtained from Gezina in Pretoria, South Africa. Prior to the extraction process, the leaves were cleaned with water to take off sand and dust. The leaves were subsequently dried out underneath sunlight for 3 days. 5 g of the dry leaves were weighed using a laboratory digital weighing scale, washed again using DW and placed in a beaker containing 100 mL of DW, which was heated to 80 °*C* for 90 min using a magnetic stirrer. A Whatman filter paper was employed to filter the extract from the leaves and the OG leaf extract was left to cool down. Finally, the leaf extract was kept for further use at 4 °*C*.

2.2. Biologic production of MNPs (Fe_3O_4 NPs)

To prepare the MNPs, a co-precipitation procedure was employed using the extract of African basil leaf as a reducing agent or organic stabilizer in this process (Mohammadi et al., 2021). 3.5 g of $FeSO_4.7H_2O$ and 6.3 g of $FeCl_3.6H_2O$ were dispersed in 100 mL deionized water in a 1:2 ratio for 30 min at 80 °C using an EINS SCI ultrasonicator. Afterwards, the leaf extract (15 mL) was included in the solution dropwise. For growth and nucleation of the Fe_3O_4 NPs while sonicating at 80 °C for

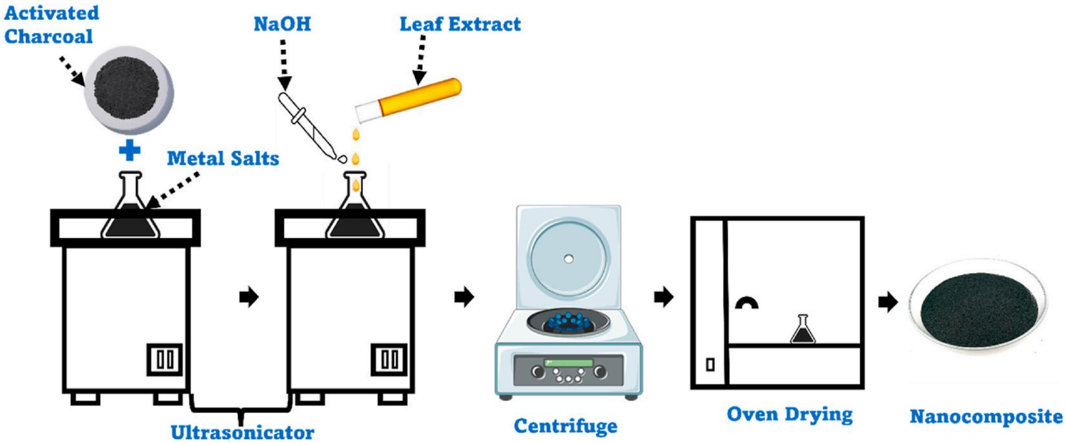

Fig. 2. Procedure for AC/Fe_3O_4 NCs production using OG leaf extract.

Table 1
Experimental scale and stages of the individual variables.

Variables	Experimental scale and levels				
	+ α (1.68)	1	0	−1	− α (− 1.68)
pH	10	8	6	4	2
Sorbent Dosage (mg)	80	65	50	35	20
Initial Concentration	300	250	200	150	100

another 30 min, 5 M of NaOH was then included dropwise till the solution pH was 11. The acquired solution was washed using DW (three times) simultaneously centrifuging at 5000 rpm for 20 min to take off impurities. The realized product was dried up in a vacuum oven at 70 °C for 24 h and was stored for further use in an airtight container.

2.3. AC/Fe_3O_4 NCs synthesis

4 g of AC and 2 g of MNPs dispersed in 100 mL DW (2:1-W/W) were sonicated for 1 h at 80 °C to produce AC/Fe_3O_4 NCs. Subsequently, 5 M of NaOH was included dropwise till the pH of the solution was 11 into the solution while sonicating at 80 °C for another 30 min for a standardized solution and accomplishment reaction. The acquired precipitate was cleaned twice with deionized water using a centrifuge operating at 4000 rpm for 15 min. The obtained precipitate was subsequently dried up at 90 °C for 24 h and kept for further use in an airtight container. Fig. 2 shows the process of producing AC/Fe_3O_4 NCs using OG leaf extract.

2.4. AC/Fe_3O_4 NCs characterization

The produced AC/Fe_3O_4 NCs were characterized using TEM (JEOL-JAPAN 200) to reveal their surface-morphology and particle size-distribution. The lattice planes were established from the selected area-electron-diffraction (SAED) pattern from TEM. An XRD spectrometry was employed (Bruker D8 focus diffractometer) to assess the

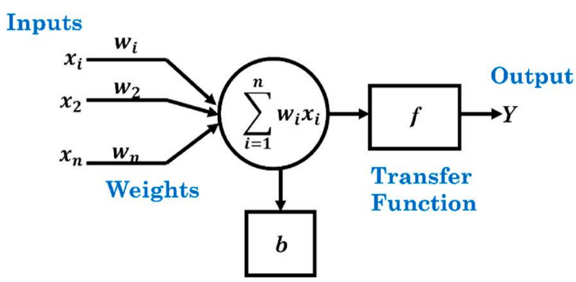

Fig. 3. ANN algorithm (KAYA and ERDEM, 2023).

Table 2
Response from adsorption experiments.

Factors	1	2	3	Response				
Run	A: pH	B: Sorbent Dosage (mg)	C: Initial Concentration (mg.L^{-1})	Removal % (Actual Value)	Predicted Value (RSM)	LM	BR	SCR
1	6	20	200	89.57	89.30	90.00	90.16	90.59
2	6	50	200	98.61	97.91	97.50	97.50	97.65
3	6	50	200	98.42	97.91	97.50	97.50	97.65
4	10	50	200	99.79	99.39	100.00	99.64	99.54
5	6	50	200	98.39	97.91	97.50	97.50	97.65
6	8	35	250	91.51	91.87	92.00	92.02	94.17
7	6	50	200	97.53	97.91	97.50	97.50	97.65
8	4	35	150	96.17	96.60	96.00	96.02	96.43
9	6	50	200	97.25	97.91	97.50	97.50	97.65
10	2	50	200	98.13	98.11	97.88	96.84	96.19
11	8	65	250	98.90	98.91	98.90	99.12	99.70
12	6	50	200	97.71	97.91	97.50	97.50	97.65
13	6	50	100	99.99	99.52	100.00	99.97	100.1
14	8	35	150	96.78	97.11	96.85	97.26	97.96
15	4	65	150	99.99	100.07	99.68	100.48	100.79
16	4	65	250	98.02	98.13	98.00	98.13	97.70
17	4	35	250	91.19	91.07	91.00	90.78	90.58
18	6	80	200	99.98	99.82	100.00	100.02	100.11
19	8	65	150	99.99	100.55	100.00	100.18	100.61
20	6	50	300	92.30	92.34	92.00	92.16	94.52

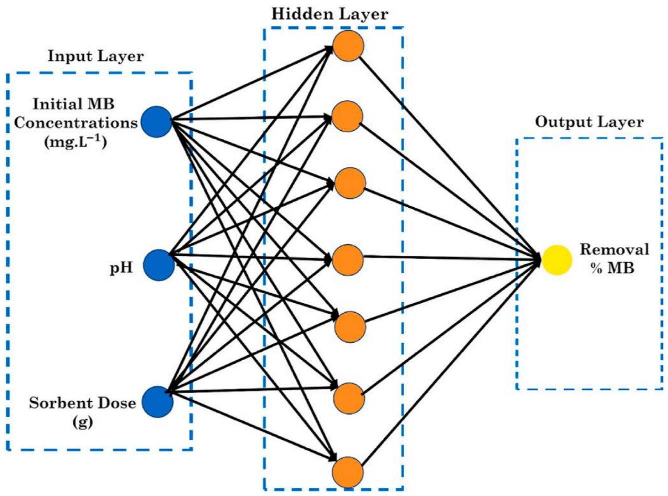

Fig. 4. The architecture of ANN.

magnetic properties of the produced AC/Fe_3O_4 NCs. FTIR spectrometry (Perkin-Elmer-Spectrum-Two-UATR) was explored to establish the functional groups of the prepared AC/Fe_3O_4 NCs. UV/Vis spectrometry (PerkinElmer SP-UV 500-spectrophotometry) was utilized to assess the optical properties of the prepared AC/Fe_3O_4 NCs.

2.5. Batch studies of MB sorption to AC/Fe_3O_4 NCs

The adsorption of MB to AC/Fe_3O_4 NCs was undertaken using the batch methodology. Based on the experimental design (Table 2), a specific dose of AC/Fe_3O_4 NCs (mg) was added to 50 mL of the desired concentration of MB solution (mg/L) at various pH and interaction times (min) and stirred at a fixed speed (rpm). For pH modification, 0.1 M NaOH and HCl were used. After a specific experiment, the retracted solution by means of a syringe was filtered through a 0.45 μm syringe filter and analyzed in a UV–Vis spectrophotometer (PerkinElmer SP-UV 500-spectrophotometry) at a wavelength of 664 nm. The percentage (%) of MB removed and equilibrium concentration (q_e) of the remaining dye in the solution was chosen as the output variable and were evaluated using Equations (1) and (2).

$$\%\ Removal = \frac{C_o - C_e}{C_o} * 100 \quad (1)$$

$$q_e = \frac{(C_o - C_e)V}{M} \quad (2)$$

C_o , C_e , V, and M indicate the MB dye initial and final concentrations ($mg.L^{-1}$), the volume of solution (L), and the sorbent dose (g).

2.6. Isotherm and kinetic studies

Isotherm studies were implemented to establish the ideal settings necessary for the sorption of MB to AC/Fe_3O_4 NCs by contacting varying concentrations of MB (100–500 $mg.L^{-1}$) with 50 mg of the sorbent at pH 10 for 60 min using a shaking speed of 250 rpm. The kinetic studies were explored by contacting 20 mg of sorbent with 100 and 150 $mg.L^{-1}$ MB concentrations at varying interaction times range of 5–60 min at pH 10 and stirring speed of 250 rpm. The q_e of dye left in the solution and the quantity of dye sorbed by unit mass of the AC/Fe_3O_4 NCs (q_t) at the time (t) ($mg.g^{-1}$) were assessed using Equations (2) and (3).

$$q_t = \left(\frac{C_o - C_t}{M}\right) \times V \quad (3)$$

V, M and C_t signifies the volume of the solution (L), the sorbent mass (g) and the concentration of dye remaining in the solution at time (t).

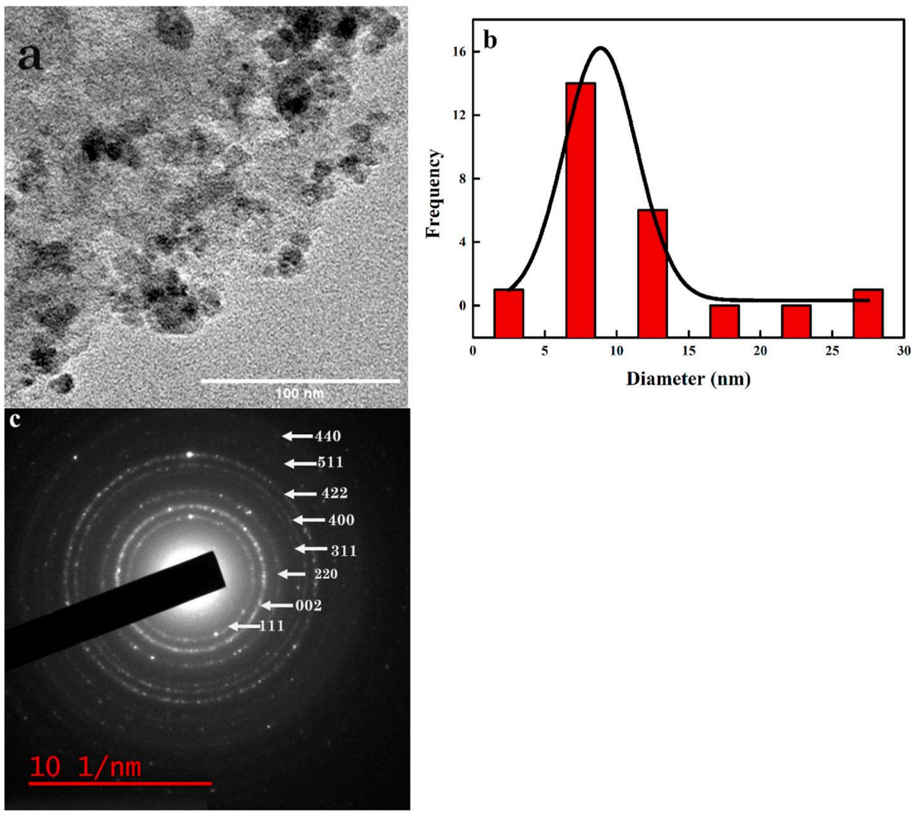

Fig. 5(a). TEM image of AC/Fe_3O_4 NCs, (b) AC/Fe_3O_4 NCs particle-size distribution and (c) AC/Fe_3O_4 NCs SAED patterns.

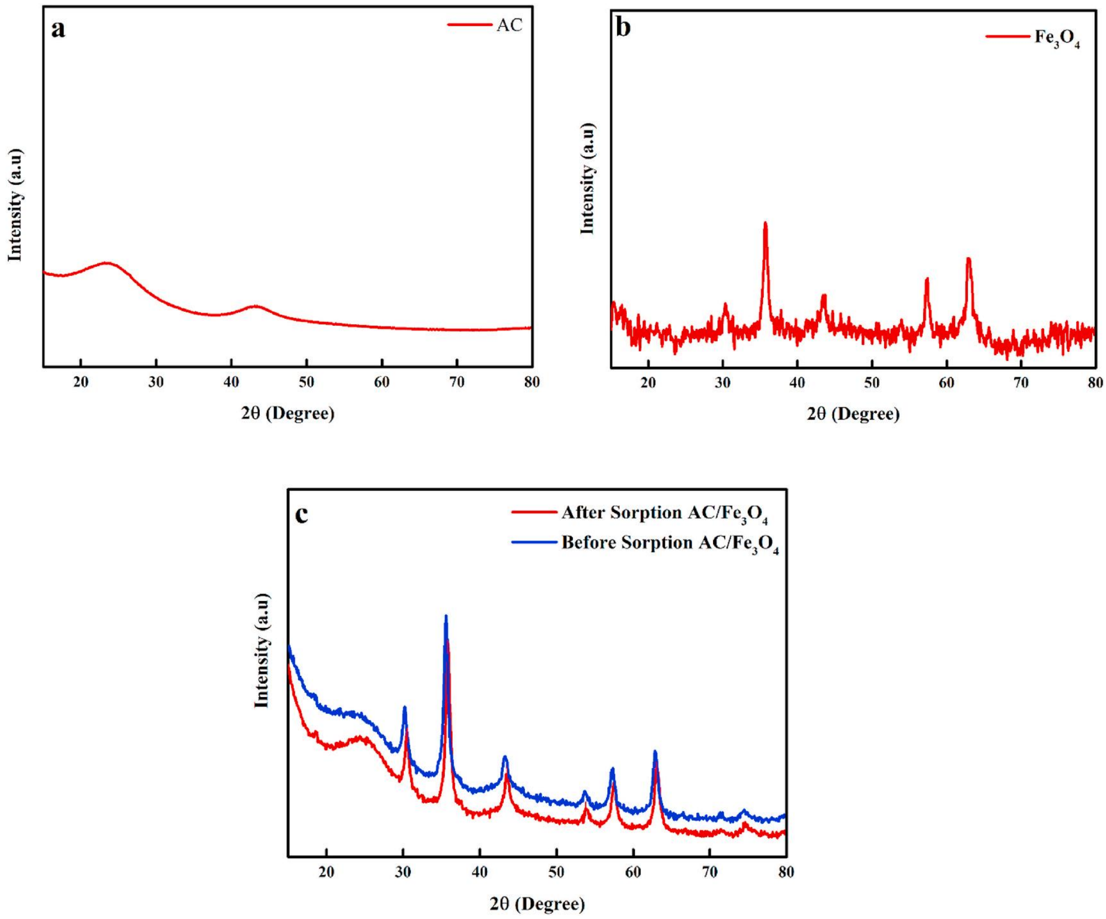

Fig. 6. XRD diffraction pattern of (a) AC, (b) Fe_3O_4 and AC/Fe_3O_4 NCs before and after sorption of MB dye.

2.7. Thermodynamic study

This was conducted to assess the impact of temperature on the sorption of MB to AC/Fe_3O_4 NCs while considering the reaction nature and practicability (Sulaiman et al., 2021; Sudarni et al., 2021). This study was performed at a temperature range of 298–313 K, by contacting 50 mg of the sorbent with 100 mg/L of MB initial concentration for 30 min interaction time and at pH 10. The equilibrium constant (K) was measured by extrapolating the Van't Hoff plot of ln (q_e/C_e) against T^{-1} to zero.

2.8. AC/Fe_3O_4 NCs point of zero charge (pH_{PZC})

AC/Fe_3O_4 NCs pH_{PZC} was established by contacting 25 mL of varied pH of 0.1 M NaCl (initial pH (pH_i)-2-12) with 20 mg of the AC/Fe_3O_4 NCs for 24 h. After 24 h, a pH-meter was utilized to measure the resulting pH (final pH (pH_f)) of the NaCl solution. The node point from the plot of pH_f against pH_i was taken as the AC/Fe_3O_4 NCs pH_{PZC}.

2.9. Design of experiment

2.9.1. RSM using the CCD for MB sorption to AC/Fe_3O_4 NCs

Active process factors optimization is critical for the sorption process. To improve the various processing variables, RSM which is a statistical technique is used (Kumari et al., 2022). The RSM is a compilation of numerical procedures that are effective in modelling and examining issues relating to the response of concern, which is impacted by various variables (Hajati et al., 2015). The design comprises of 2k factorial factors enhanced by 2k axial factors and centre factors where k is the sum of variables. The three operating variables coded values (A, B and C), were set at five stages with +1.68 (highest stage), 1, 0, −1, and −1.68 (lowest stage) as depicted in Table 1. The five stages were evaluated centred on the full-face-centred CCD experimental strategy. Hence, 20 sets of experiments were conducted and systematized in a factorial design (8 factorial points, 6 axial points and 6 centre points) using Equation (4).

$$2^k + 2k + 6 \qquad (4)$$

k represents the number of factors (Moradi et al., 2016).

Sorption experiments were implemented by simultaneously optimizing three variables (pH, sorbent dosage, and initial dye concentration). A full 20-factorial design with 5 central points was explored in this study using Design Expert 13 software. The response of the factorial design based on the % of dye molecules eliminated and the q_e are displayed in Table 2. The acquired experimental information was exposed to a second-order polynomial regression model, and the response (Y) was associated with the self-determining variables as a polynomial model centred on the quadratic equation given by Equation (5).

$$Y = \beta_o + \sum_{i=1}^{3}\beta_i x_i + \sum_{i=1}^{3}\beta_{ii}x_i^2 + \sum_{i=1}^{2}\sum_{j=i+1}^{3}\beta_{ij}x_i x_j + e \qquad (5)$$

x_i, x_j, β_o, β_i, β_{ii}, β_{ij}, and e represents the real variables, coded variables of MB solution pH, AC/Fe_3O_4 NCs and initial MB concentration, intercept, quadratic, linear and interaction impacts and error (Igwegbe et al., 2019; Pekdemir et al., 2022; Hanafi et al., 2022).

2.9.2. ANN modelling

Various ANN applications are accomplished in environmental

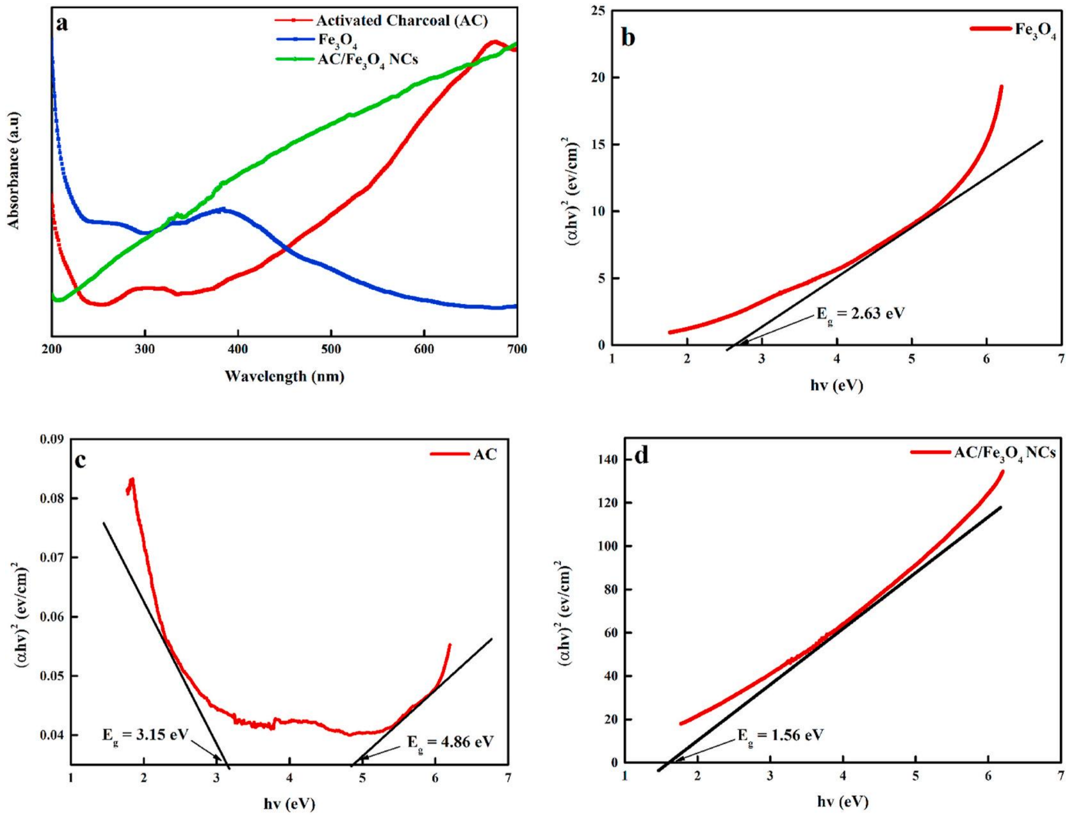

Fig. 7. UV spectra of (a) AC, Fe_3O_4 NPs and AC/Fe_3O_4 NCs, and the determined bandgap of (b) Fe_3O_4 NPs, (c) AC and (d) AC/Fe_3O_4 NCs.

engineering like function estimation, pattern identification, and classification (Khan et al., 2017). Computer technology advancements in modern times have enhanced artificial intelligence study's interest. Information processing principles of humans and imitating the functioning of biologic nervous systems observation are the key goals of artificial intelligence study. ANN is a reasonable programming form created by replicating the human brain's working mechanisms. It is a learning algorithm that can function with the human brain in the computer background, make decisions and reach the result by employing the existing data in the instance of inadequate information (Altintig et al., 2023).

ANN is well recognized for its superior capacity to learn and classify data. The idea of ANN comes from the research on the function and structure of the brain and nervous and the learning and responding process (Khan et al., 2017). Furthermore, to the input and output layers, most ANN models have one or added hidden layers, and the numeral is influenced by the study classification. ANN's key attribute is its capability to execute core computations to assess the trained output from the input data. It is dependable and effective in showcasing the NL interactions between the variables and distinct process responses, they may be applied in complex systems. ANN can also evaluate multi-factorial NL and complex processes given enough information via training in multiple input-output network algorithms (Banza et al., 2023a).

ANN have a comparable structure depicted in Fig. 3, where inputs to the neuron and the output are x_i (i = 1, 2, … … n) and Y. Individual weight is augmented by its weight (w_i), and the individual neuron is linked with a bias b and their computation goes via a transfer function f. Hence, the association between the input and output is defined by Equation (6). Some neurons are linked to outer space to obtain inputs and transfer output in this structure. The hidden layer comprises of residual neurons, which have connections only within the network. The input and output layers are comprised of a sole layer, and between two layers, there may be more than one hidden layer. These hidden layers comprise of a huge number of neurons, and these neurons are generally linked with other neurons in the networks (KAYA and ERDEM, 2023).

$$Y = f\sum_{i=1}^{n}(w_i x_i + b) \quad (6)$$

The NN is trained through a feed-forward and backpropagation (BP) procedure to determine an association between the input and the output metadata, assessing the error linked with the modelling and predicting potential precise responses. Independent variables are fed to the input layer and the responses/dependent variables are included in the output layer. The input layer is regarded as inactive as no processing takes place. The synaptic weights which possess data relevant to the ANN are used to transmit information to the outer layer alongside the hidden layer (Makomere et al., 2023).

They are deemed as a NL approach for determining an association between the independent and dependent variables. The following steps are involved in ANN model configuration procedures: data collection, set selection training and testing, data conversion into ANN inputs, network structure identification, training and testing and repeating the procedures several times to get the best model if necessary (Banza et al., 2023b). Fig. 4 shows the network architecture employed for this study. In this study, a three-layered BP NN was employed. It has a linear transfer function (purelin) at the output layer and a tangent sigmoid transfer function (tansig) at the hidden layer. ANN modelling of MB sorption to AC/Fe_3O_4 NCs was explored utilizing 20 experimental data sets, which was achieved by performing the NN function in MATLAB R2018b scientific software. The experimental data is grouped into the input-matrix and target or output-matrix. The input-variables in this study were the pH, sorbent dosage and original MB concentration. While the % of MB removed was utilized as the target or output. The data clusters were separated into 70% (training), 15% (validation) and (15%) testing (Khan et al., 2017).

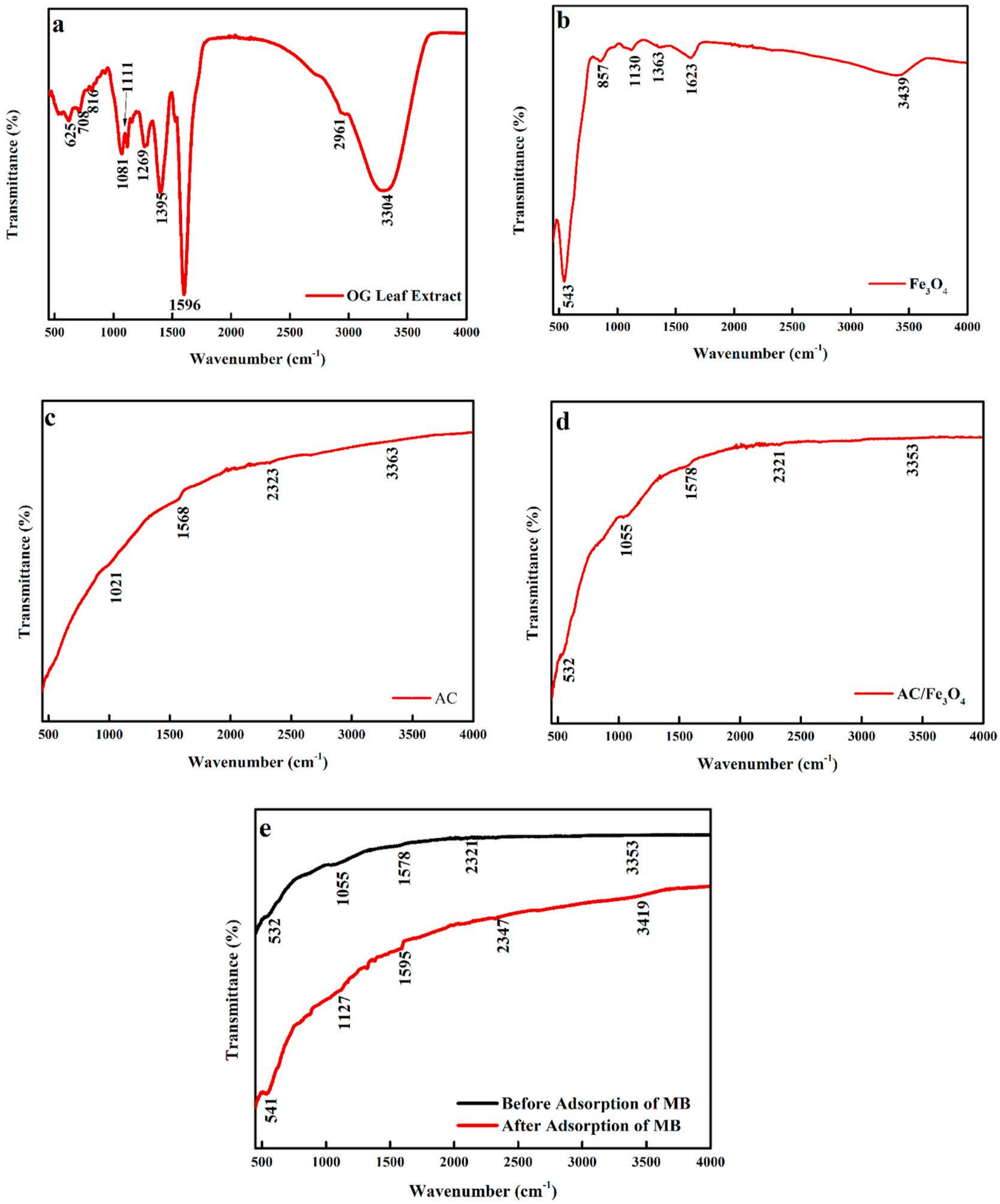

Fig. 8. IR spectra of (a) OG leaf extract, (b) Fe_3O_4 NPs, (c) AC, (d) AC/Fe_3O_4 NCs and (e) AC/Fe_3O_4 NCs before and after sorption of MB dye.

2.9.3. Error-analysis associated with kinetic and isotherm studies

For evaluating parameters of the kinetic and isotherm models, among the number of techniques conceived and highly used is the linear regression technique. The linear regression technique is a traditional technique of parameter assessment grounded on the Gaussian distribution of error theory at individual statistics points. That entails the NL-equations linearization for the assessment of the most excellent fit terms. Yet, such conversion of the NL equations into linear states is indirectly linked with specific modifications in error structure and may defy the error adjustment as well as normality theory. Hence, the inadequate applicability of linear regression for the approximation of only two variables in an experimental calculation (Ayawei et al., 2017).

A further complex, yet exact technique for the evaluation of isotherm and kinetic parameters, which needs an error function estimation to measure the ideal fit of the parameters to the experimental results is the NL method of optimization. But every one of the error function evaluations results in various sets of parameters. Also, the error distribution in the NL technique is not transformed as in the linear regression method. To effectively placate this, the non-linearized chi-square (X^2) was used alongside RSS and was explored for the assessment of the ideal fit for the kinetic and isotherm models, to provide a comprehensive sorption mechanism for theoretical assessment, designing and evaluating the sorption system for an experimental application in this study the origin lab version 9 software was used (Dubey et al., 2016). The NL isotherm and kinetic models were employed to estimate the relationship relating to the model-calculated data and the experimental data using the X^2 and RSS error analysis (Equations (7) and (8)) (Hashem et al., 2022).

$$X^2 = \sum_{1=0}^{n} \frac{\left(q_{e(cal)} - q_{e(meas)}\right)^2}{q_{e(meas)}} \quad (7)$$

$$RSS = \sum_{i=1}^{n} \left(q_{e(exp)} - q_{e(cal)}\right)_i^2 \quad (8)$$

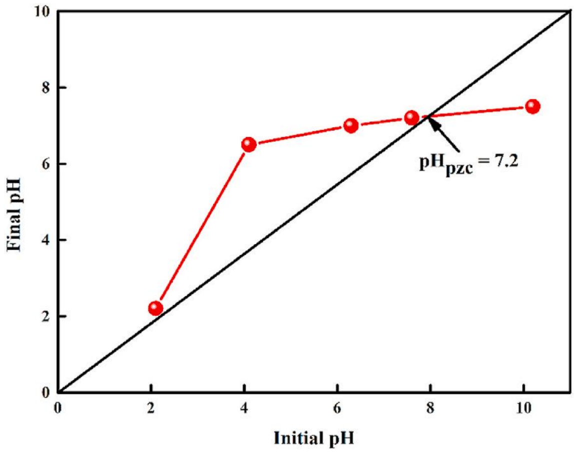

Fig. 9. The plot of the pH_f against the pH_i (experimental conditions: pH-2-10, dosage 20 mg, concentration-0.1 M NaCl, interaction time-1440 min).

n, q_e(cal) and q_e(meas) represent the sum of experiments carried-out, the amount of sorbate achieved by the isotherm and kinetic models (mg. g^{-1}) and the amount of sorbate adsorbed by the sorbent during the experiment (mg.L^{-1}) (Ayawei et al., 2017).

2.9.4. Assessment of model performance criteria for ANN

Model assessment can be carried out via error statistical scrutiny. Results of the model-predicted were assessed using the mean-square-error (MSE), root MSE (RMSE) and the coefficient of regression (R^2), which are achieved by using Equations (9)–(11) to validate the model. The superlative model performance is the structure where MSE and RMSE approach 0 and R^2 value approaches 1.

$$MSE = \frac{1}{n}\sum_{i=1}^{n}\left(X_p - X_e\right)^2 \quad 9$$

$$R^2 = 1 = \frac{\sum_{i=1}^{n}\left(X_p - X_e\right)^2}{\sum_{i=1}^{n}\left(X_p - X_m\right)^2} \quad 10$$

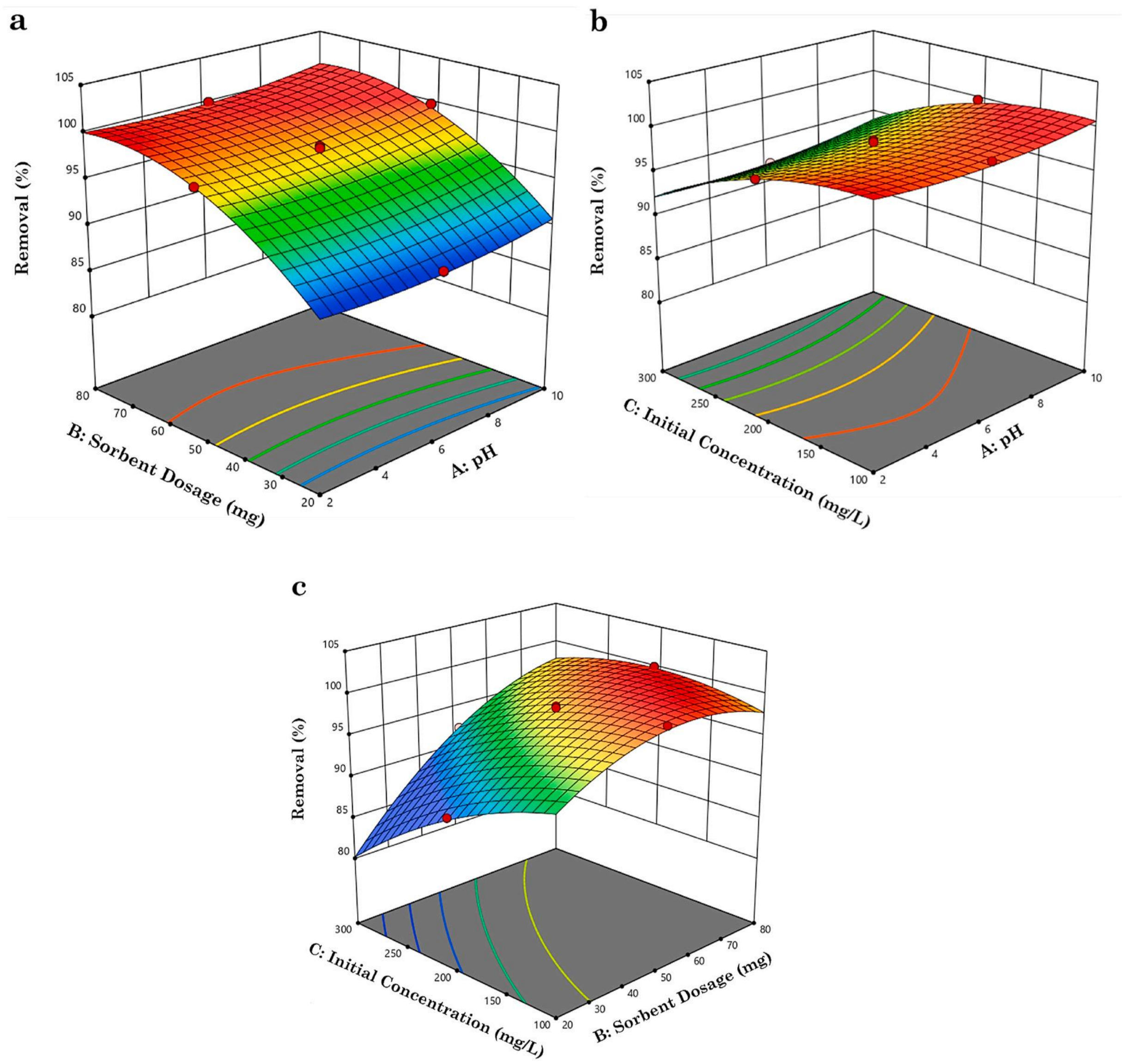

Fig. 10. 3-D plots of MB confiscation (a) pH and sorbent dosage (b) pH and initial concentration and (c) sorbent dosage and initial concentration (experimental conditions: pH-2-10, sorbent dosage-20-80 mg, initial concentration-100-300 mg.L^{-1}, and interaction time-120 min).

Table 3
ANOVA and coefficients model for the MB elimination.

Source	Sum of Squares	df	Mean Square	F-value	p-value	
Model	195.86	9	21.76	76.38	<0.0001	Significant
A-pH	1.64	1	1.64	5.77	0.0372	
B-Sorbent Dosage	110.57	1	110.57	388.07	<0.0001	
C-Initial Concentration	51.51	1	51.51	180.78	<0.0001	
AB	0.0004	1	0.0004	0.0014	0.9714	
AC	0.0423	1	0.0423	0.1484	0.7081	
BC	6.45	1	6.45	22.64	0.0008	
A^2	1.10	1	1.10	3.85	0.0783	
B^2	17.66	1	17.66	61.98	<0.0001	
C^2	6.16	1	6.16	21.61	0.0009	
Residual	2.85	10	0.2849			
Lack of Fit	1.28	5	0.2566	0.8191	0.5840	Not significant
Pure Error	1.57	5	0.3133			
Cor Total	198.71	19				

Table 4
Fit statistics of MB confiscation.

Std. Dev.	0.5338	R^2	0.9857
Mean	97.01	**Adjusted R^2**	0.9728
C.V. %	0.5502	**Predicted R^2**	0.9378
		Adeq Precision	29.8107

$$\text{RMSE} = \sqrt{\frac{1}{n}\sum_{i=1}^{n}\left(X_p - X_e\right)^2} \quad (11)$$

X_p, X_e, X_m and n represent the predicted and actual/experimental values, the average of the experimental data and the number of data sets (KAYA and ERDEM, 2023; Ahmad et al., 2020; Makomere et al., 2023; Prasad and Yadav, 2020; Kakhki et al., 2020).

3. Results and discussions

3.1. TEM analysis

The TEM image of the prepared AC/Fe_3O_4 NCs is illustrated in Fig. 5a. The image shows a nearly regular distribution of dispersed spherical MNCs particles. The particle size diameter extended from 4-9–28.7 nm, with an average particle size of approximately 8.9 ± 3.0 nm (Fig. 5b), obtained by curve fitting of the plot using the Gaussian distribution function in Originlab software. While Fig. 5c shows AC/Fe_3O_4 NCs SAED patterns which match the MNCs diffraction planes. The figure also shows the polycrystalline nature of the TEM image with concentric fuse diffraction rings and several bright spots. The computed lattice spacing from the SAED patterns were 0.5548, 0.2850, 0.1931, 0.1614, 0.1389, 0.0999 and 0.0744, which corresponds to 111, 220, 311, 400, 422, 511 and 440 of Fe_3O_4 diffraction planes. While 0.4061 estimated lattice spacing corresponds to 002 planes of disorder carbon of charcoal. These findings are in good standing with the diffraction planes estimated from XRD patterns (Ahmed and Ahmaruzzaman, 2015).

3.2. XRD analysis

The XRD diffraction peaks observed at 2θ = 23.5° and 43.3° correspond to the reflection planes of 002 and 100 of a characteristic of the non-crystalline structure of AC (JCPDS 00-056-0159) (Fig. 6a) (Rodrigues et al., 2020; Sonal et al., 2020; Raj and Joy, 2015; Keppetipola et al., 2021). While the peaks noticed at 2θ = 21.6°, 30.3°, 35.7°, 43.5°, 53.8°, 57.5°, and 62.9° with corresponding diffraction planes of 111, 220, 311, 400, 422, 511 and 440 were attributed to Fe_3O_4 standard peaks (JCDDS No. 190629) Fig. 6b (Hamedi et al., 2019; Lopes et al., 2021). Fig. 6c represents the XRD of AC/Fe_3O_4 NCs, which shows the standard diffraction peaks of Fe_3O_4 and amorphous AC. After the sorption of MB dye, an observed reduction in the intensity of the diffraction peaks was noticed, which was suggestive of the MB dye molecules' sorption into pores of the AC/Fe_3O_4 NCs via the physisorption process. The crystalline size of Fe_3O_4, and AC/Fe_3O_4 NCs before and after the sorption of MB dye was evaluated using the Debye Scherrer equation (Equation (12)) from the utmost intense diffraction peaks, where λ is the monochromatic X-ray beam wavelength, B is the Full-Width at Half-Maximum (FWHM) of the XRD peak at the optimum intensity, θ is the angle of peak diffraction that satisfies the Bragg's law for the h k l plane and C $_{(hkl)}$ is the crystallite-size (Nistor et al., 2021).

$$C_{(hkl)} = \frac{0.9\lambda}{B\cos\theta} \quad (12)$$

The obtained crystallite size calculated from the (311) diffraction peak for Fe_3O_4 and AC/Fe_3O_4 before and after sorption of MB dye was established to be 11.15, 14.27 and 13.98 nm. There was an observed reduction in the intensity of the diffraction peaks and the crystalline size of the AC/Fe_3O_4 NCs after the biosorption of MB dye, as depicted in Fig. 6c. Shift in the diffraction peaks was also noticed after sorption of MB dye using AC/Fe_3O_4 NCs was ascribed to unit cell contraction (Rout et al., 2015).

3.3. UV analysis

The UV spectrum attained for AC, Fe_3O_4 NPs and AC/Fe_3O_4 NCs was assessed at a wavelength array of 200–700 nm. The observed adsorption peak of 310 nm was ascribed to AC (Fig. 7a). While the adsorption peaks noticed at 261, 334 and 388 nm are ascribed to the composition of the capped polyphenols, and flavonoids by the OG leaf extract and trivalent iron site on Fe_3O_4. After the fusion of AC into Fe_3O_4, three adsorption peaks were noticed at 297, 331 and 382 nm, there was a decrease in the observed adsorption peaks which were attributed to AC, OG leaf extract and trivalent iron site on Fe_3O_4 (Fig. 7a) (Prasad, 2016).

The material response owing to electromagnetic radiation, especially visible light was analyzed from the optical properties. From the viewpoint of quantum mechanics, electromagnetic radiation is deemed as an energy type named photon and the photon energy is quantized via Planck's principle given by Equation (13).

$$E = h\nu = \frac{hc}{\lambda} \quad (13)$$

h, c, and λ describe the Planck-constant (6.63×10^{-34} J/s), speed of light in vacuum, and the wavelength of a photon. The scrutiny of the α data in reaction to the wavelength in the assessment of the optical-bandgap is observed to be reliant on Tauc's Equation (14).

$$(\alpha h\nu)^{\frac{1}{\gamma}} = B\left(h\nu - E_g\right) \quad (14)$$

hν, B, E_g and γ denote the photon energy (eV), band type factor, optical

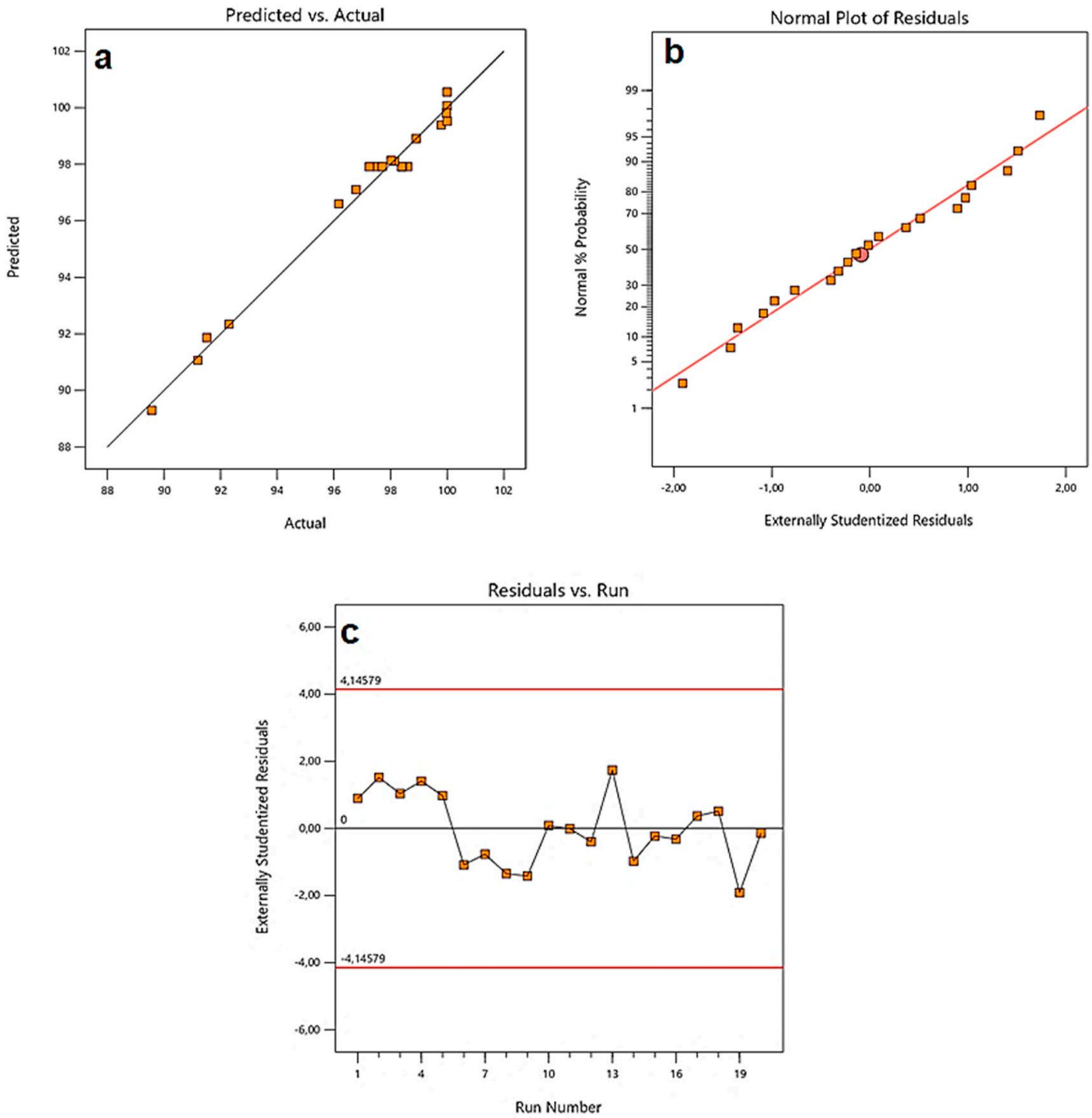

Fig. 11. Plots of (a) predicted vs. actual (b) normal plot of residuals and (c) residual vs. run of MB elimination.

energy bandgap and the direct (1/2) and indirect (2) permitted transitions (Hussein et al., 2020). From the plots of $(\alpha h v)^2$ against hv in Fig. 5b-c, three values of E_g for Fe_3O_4 NPs, AC and AC/Fe_3O_4 NCs were determined to be 2.63 eV, 3.15–4.8 eV and 1.56 eV.

3.4. FTIR analysis

The FTIR spectra of OG leaf extract, Fe_3O_4 NPs, AC, and AC/Fe_3O_4 NCs before and after the sorption of MB dye are presented in Fig. 8. The characteristics peaks observed at 3304, 2961, 1596, 1444,1395-1111, 1081, 816, 708 and 625 cm^{-1} were credited to the O–H group of carboxylic acid group, C–H stretching of alkanes, N–H/C–N stretching of protein, C–H bending, C–H stretching of alkanes, PO^{2-} symmetric stretch (mainly nuclei acids), C–H bending of methyl glycogen, CH_2 bending of carbohydrate, protein and lipids, C–*O*–O or P–*O*–C bonding of phosphate of OG leaf extract (Fig. 8a). The projecting protein peaks found in the 3304 and 1596 cm^{-1} were from the leaf extract which acted as a reducing agent in the reduction of Fe ions to Fe_3O_4 NPs (Selvaraju et al., 2021; Raju et al., 2017; Karthik et al., 2020; Blessing et al., 2017; Kristianto et al., 2016). The band at 543 cm^{-1} in Fig. 8b is consistent with FeO stretching vibration at the octahedral site of iron (III) oxide. While the bands at 3439, 1623, 1363, 1180 and 857 cm^{-1} in Fig. 8b were ascribed to the O–H group of the phenol, carboxyl C–O stretching of lipid, C–H stretching, CH deformation, C–O and C–C stretching of carbohydrates and C–Cl stretching of halogen compounds (Prasad, 2016; Karthik et al., 2020; Udunwa et al., 2017). The band at 1568 cm^{-1} was ascribed to C═C stretching vibration in the aromatic ring mostly observed in carbonaceous material like AC. While the bands at 1021, 2321 and 3363 cm^{-1} were also attributed to C–O bending (OH), the existence of symmetric and asymmetric C–H stretching vibration of hydrocarbon structure and O–H stretching vibration owing to inter-molecular hydrogen bonding of polymeric compounds such as phenols, alcohols, and carboxylic acids which indicate the free OH groups present on the carbon surface (Fig. 8c). After the fusion of AC into Fe_3O_4, an additional band at 532 cm^{-1} which relates to FeO stretching vibration was noticed in Fig. 8d (Gupta et al., 2021; Joshi and Pokharel, 2013; Ali et al., 2020; Saafie et al., 2019). After the sorption of MB dyes to AC/Fe_3O_4 NCs, there was no significant change in the observed bands, which was indicative of the dye removal main mechanism due to ion exchange between the negatively (-ve) charged groups of AC/Fe_3O_4 NCs and the cationic dye molecules (Seoane et al., 2022). There was a red shift in all bands after the adsorption of MB dyes to 541, 1121, 1595, 2347 and 3419 cm^{-1} and these correspond to the functional groups of FeO stretching vibration, C–O bending (OH), C═C stretching vibration

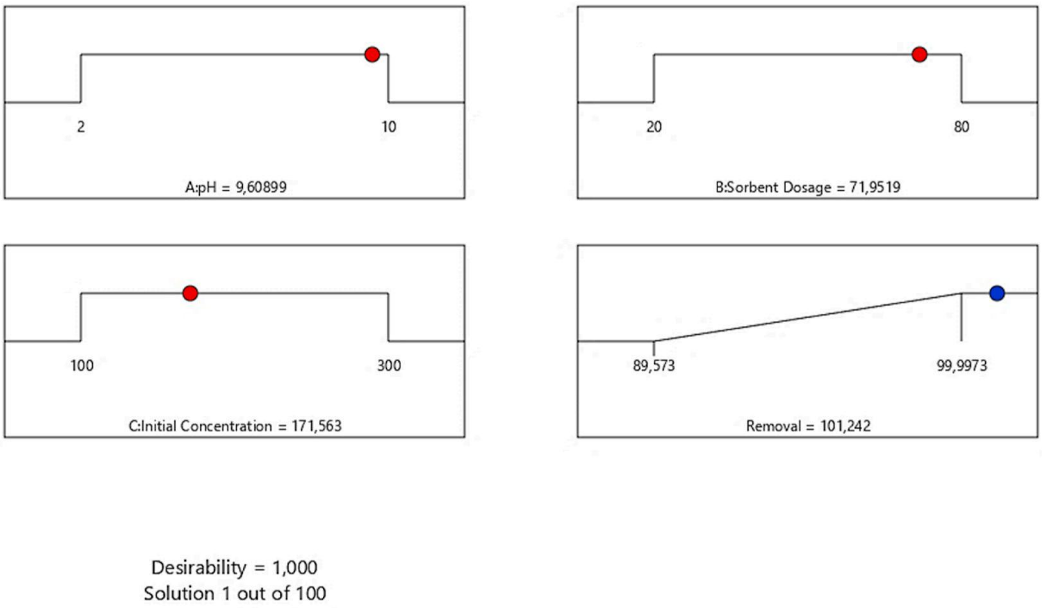

Fig. 12. DF of MB elimination.

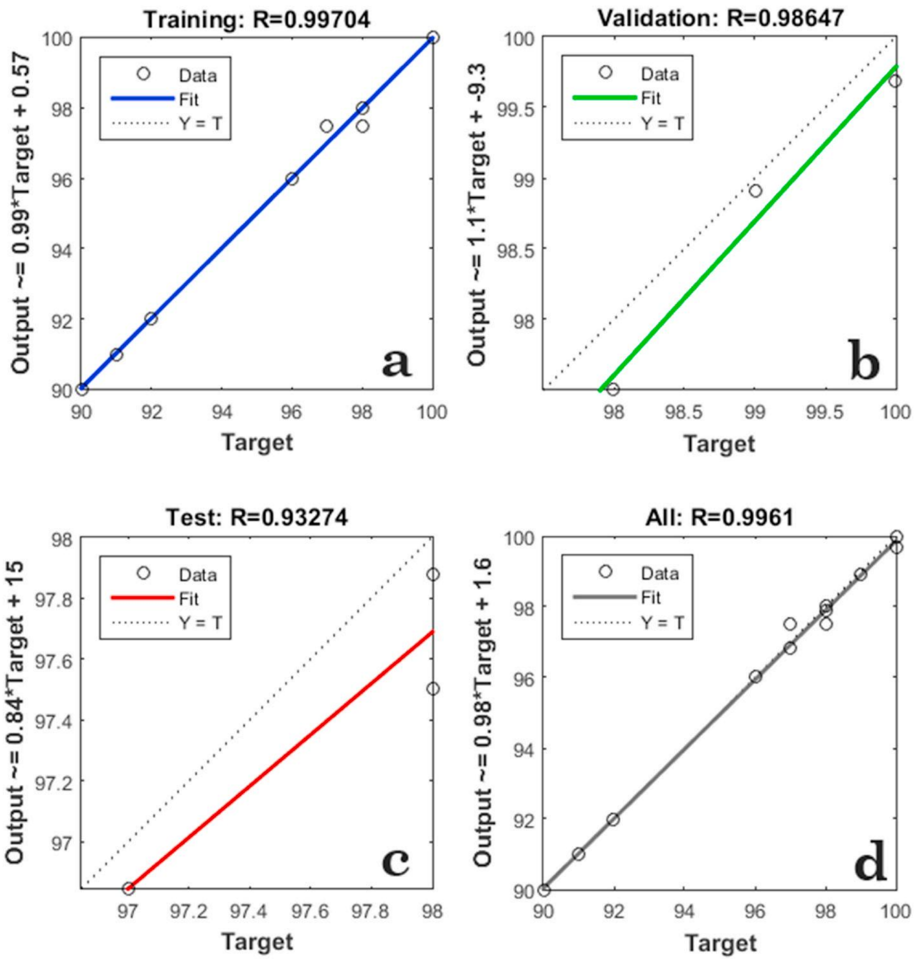

Fig. 13. LM regression plots using (a) training, (b) validation, (c) testing and (d) complete data for AC/Fe_3O_4 NCs sorption of MB dyes.

in the aromatic ring, the existence of symmetric and asymmetric C–H stretching vibration of hydrocarbon structure and O–H stretching vibration owing to inter-molecular hydrogen bonding of polymeric compounds such as phenols, alcohols, and carboxylic acids which indicate the free OH groups present on the carbon surface (Fig. 8e).

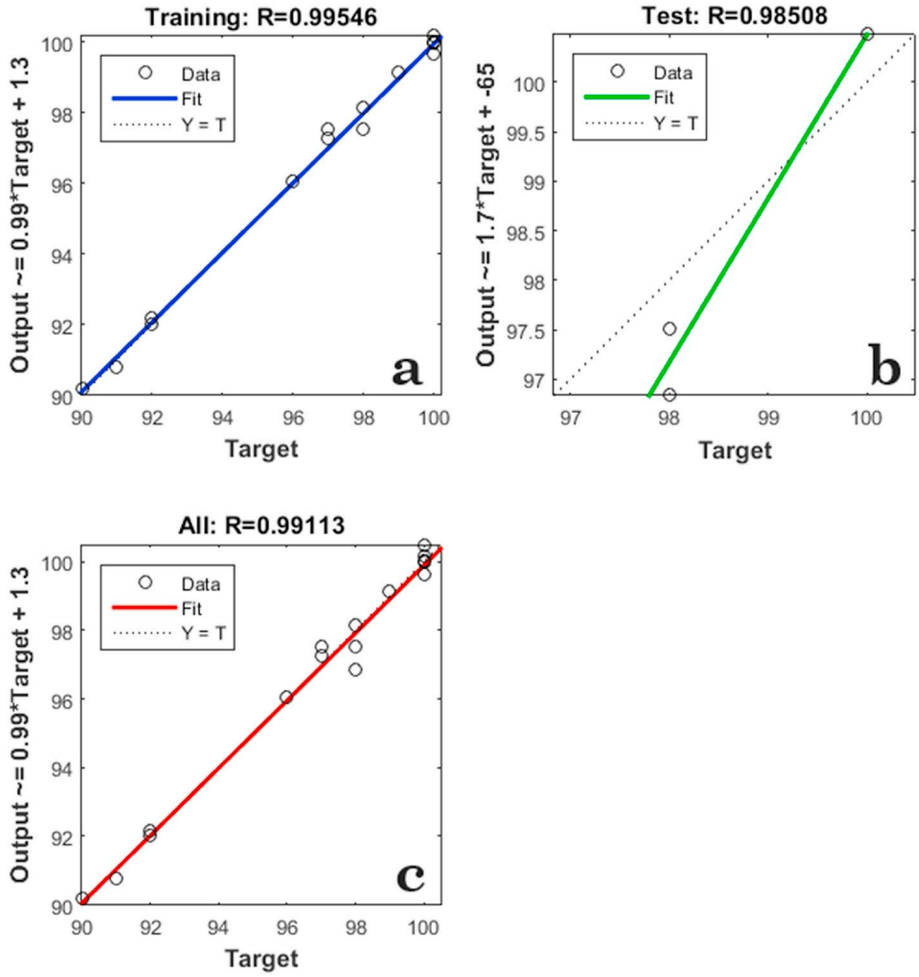

Fig. 14. BR regression plots using (a) training, (b) testing and (c) complete data for AC/Fe_3O_4 NCs sorption of MB dyes.

3.5. pH_{PZC} of AC/Fe_3O_4 NCs

The sorption of ionic compounds is critically impacted by the solution pH. Hence, sorbent pH_{PZC} determination is vital and dependable for favourable or unfavourable sorption processes (Seoane et al., 2022). The pH_{PZC} of AC/Fe_3O_4 NCs was 7.2 as depicted in Fig. 9. At pH < pH_{PZC} of AC/Fe_3O_4 NCs (acid conditions), the surface of the NCs was positively (+ve) charged and at pH > pH_{PZC} of AC/Fe_3O_4 NCs, the surface of the NCs was -ve charged, thereby sorb the anionic MB dye molecules effectively.

3.6. Influence of process variables on sorption of MB to AC/Fe_3O_4 NCs

The advantage of utilizing the RSM is the creation of 3-D plots, which assist in recognizing the impacts of process variables interactions on the process result (Natrayan et al., 2022; Kusuma et al., 2023). A critical parameter in verifying the possibility of the sorption of anionic and cationic organic dye compounds is the pH (Ouldmoumna et al., 2013; Elwakeel et al., 2018). The pKa of MB is 3.5 and it is fully ionized at pH > 3.5, hence occurring under a cationic form (Igwegbe et al., 2019). Results of the sorption of MB as a function of pH and dosage are depicted in Fig. 10a. As observed in Fig. 10a, the sorption of MB dye increased with increasing pH and sorbent-dosage, with optimum sorption observed at pH 10 employing 50 mg of sorbent dosage. This was accredited to the electrostatic interaction between the deprotonated sites on the sorbent, which was -ve charged at pH > 7.2 and the cationic dye molecules. At low pH, the sites on the sorbent were protonated (H^+) leading to electrostatic repulsion between the dye molecules and the +ve charged sites on the surface of the sorbent. Also, it was noted in Fig. 10aa, that the % of MB dye confiscated to the NCs increased with increasing sorbent dosage used.

Fig. 10b displays the influence of pH and initial MB concentration on the % of MB confiscated to the NCs. With the improvement in the pH of the solution with increasing initial MB concentration, a decrease in the % of MB confiscated to the NCs was noticed. The initial MB concentration had a negative influence on the confiscation of MB dye molecules, with improved initial MB concentration from 100 to 300 $mg.L^{-1}$ led to a reduction in the % of MB confiscated from 99 to 92%. This behaviour is associated with the viable sorption of dye molecules complication at various concentrations on the NCs surface. At elevated concentrations, the sorbent surface gets saturated resulting in the reduction of the % of MB confiscated (Alipour et al., 2022).

Fig. 10c exhibits the influence of sorbent dosage and initial MB concentrations on the % of MB confiscated to AC/Fe_3O_4 NCs. It was noticed in this study that there was an improvement in the % of MB dye molecules confiscated to NCs as the sorbent dosage was increased with intensifying initial MB concentrations and was ascribed to the increased accessibility of sorption sites/surface area for the confiscation of MB dye molecules. A further increase in the sorbent dosage above 60 mg (sorption equilibrium), did not result in a further upsurge in the rate of MB confiscated as the MB concentration was intensified (Alipour et al., 2022).

3.6.1. CCD and ANOVA test

ANOVA test was explored to determine the interaction between the response and process variables and the fit polynomial model quality is

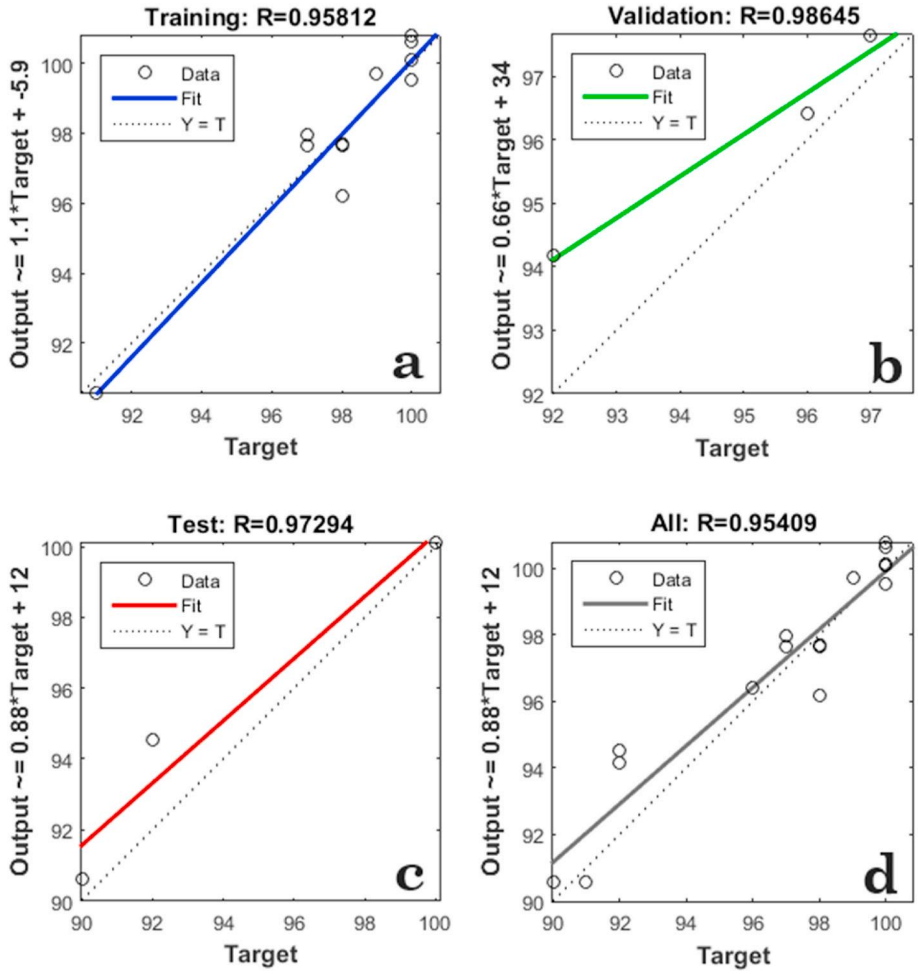

Fig. 15. SCG regression plots using (a) training, (b) validation, (c) testing and (d) complete data for AC/Fe_3O_4 NCs sorption of MB dyes.

communicated by the coefficient of determination (R^2). The P-value (probability) with a 95% level of confidence was employed to assess the model term and ANOVA for the % removal (Y) is represented by Table 3. Parameters of the quadratic models (Table 3) were considerable at the 5% confidence intervals as the P-values were < 0.05 (significant model terms were A, B, C, BC, B^2 and C^2 and insignificant model terms were AB, AC, and A^2) and the R^2 value was 0.9857, which was > 0.80, which is the limit for a good fit model. A high R^2 value guarantees a suitable variation of the quadratic model to the experimental data and shows a good pact between the observed and calculated outcomes. Also, an extreme R^2 value shows a desired and rational pact with the adjusted R^2 value. When the P-value of the model term is > 0.05, they are well thought out to have inadequate influence, hence they must be expected to enhance the models from the research. The predicted R^2 value (0.9378) was in realistic pact with the adjusted R^2 value (0.9728) and the difference between the adj and predicted R^2 values was 0.03, which validates decent certainty of the model (difference should be < 0.2) (Table 4) (Alipour et al., 2022; Zhao et al., 2022). Thus, the selected model was satisfactorily correct for MB confiscation and gives an excellent projection of the outcome. Also, the equation of the prediction of the % of MB confiscated is given by Equation (15). The degree of the signal-to-noise ratio was assessed using the Adeq Precision and an adequate signal of a ratio of 29.811 was suggestive and desirable for the experimental runs, as it was a ratio > 4 (Table 4). This model can be employed to traverse the model space. Furthermore, owing to the low C.V value of 0.5507, the model was highly functional.

$$\%\,\text{Removal} = 92,7891 + -0,599848 * \text{A} + 0,309676 * \text{B} + -0,0209376 * \text{C} + -0,000231389 * \text{AB} + 0,000727083 * \text{AC} + 0,00119726 * \text{BC} + 0,0521895 * \text{A}\hat{2} + -0,00372485 * \text{B}\hat{2} + -0,000197932 * \text{C}\hat{2} \quad (15)$$

To assess the validation of model adequacy, the diagnostic plots in Fig. 11a-c were employed. Fig. 11a shows that the actual and predicted removal of the MB plot fitted well to linear regression, indicating that the model was adequate in describing the experimental terms. Fig. 11b shows the normal plot of residuals (externally studentized residual against the % of normal probability), which was appropriate for outlier detection. The normal error distribution across all runs and the model adequacy for this experiment were deduced from the linear point distribution in the plots. Fig. 11c shows the plot of residual against the run plot, where the points standing away from the red threshold are considered as the outliers. None of the points in Fig. 11c was observed to be outside the limit of the model expectations, which was suggestive of no more outliers being obtainable (Zenebe et al., 2021; Rosly et al., 2021).

The desirability function (DF) was employed to approximate the most excellent predicted prospect for the maximum response (Kumari et al., 2022). For the optimization process, the DF was utilized, and this varies from 0 (undesirable) to 1 (desirable). The statistical optimization technique gets the points that boost the preferred function. The most excellent forecast values for the optimum % of MB confiscated and the DF is displayed in the optimization plot in Fig. 12. The ideal predicted condition for the optimal confiscation of MB using the DF was pH of 9.6,

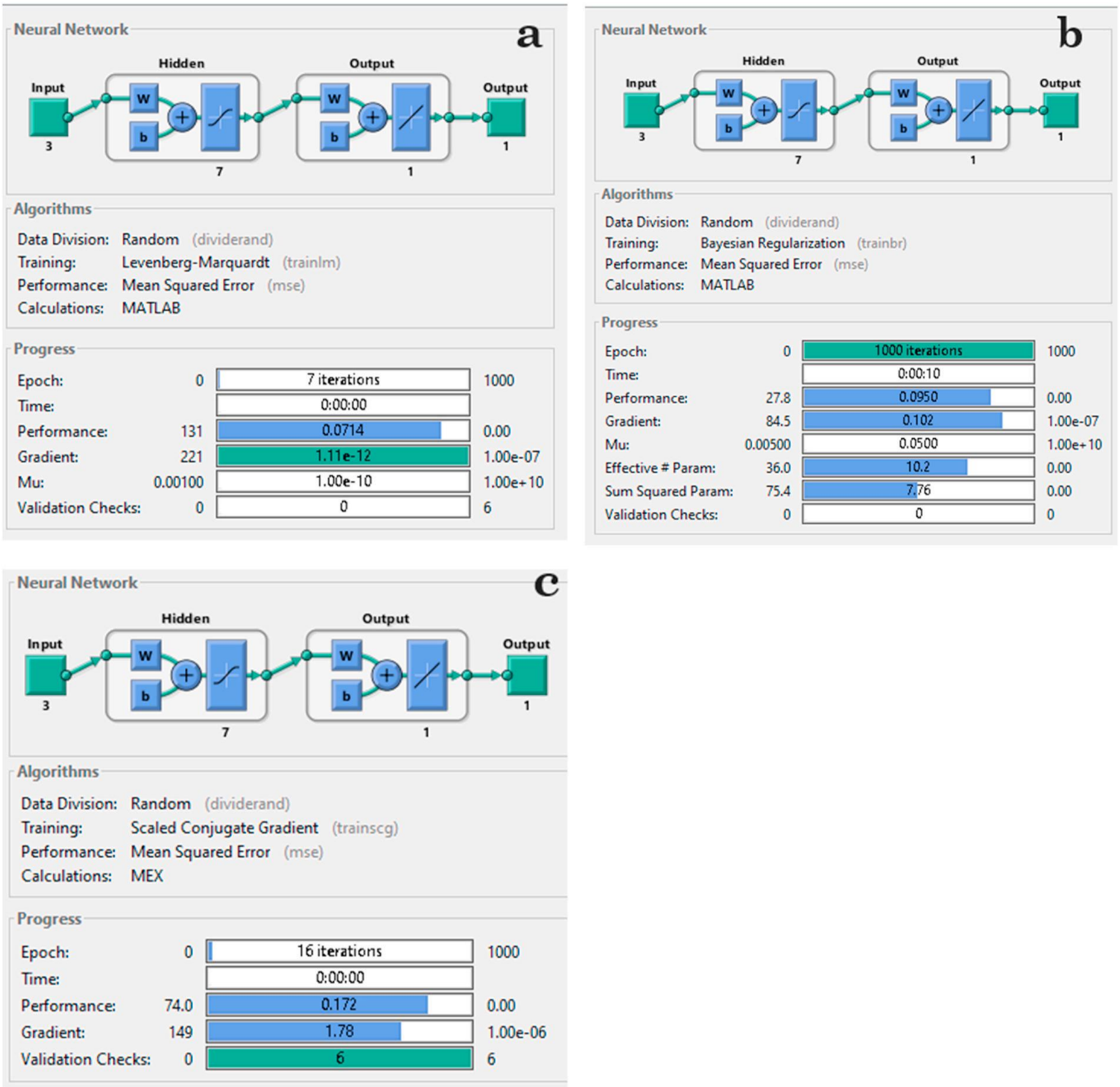

Fig. 16. ANN Toolbox for MB removal using AC/Fe_3O_4 NCs.

Table 5
ANN functioning using hidden node structure.

	LM			BR			SCG		
	MSE	RMSE	R^2	MSE	RMSE	R^2	MSE	RMSE	R^2
Training	0.0714	0.2672	0.9970	0.0950	0.3082	0.9955	0.5069	0.7120	0.9581
Validation	0.0120	0.1096	0.9865	0.0000	0.0000	0.0000	1.7737	1.3318	0.9865
Testing	0.0964	0.3105	0.9327	0.6111	0.7817	0.9851	2.2390	1.4963	0.9729

sorbent dosage of 71.95 mg, initial MB concentration of 171.56 mg.L^{-1} and % of dye confiscated was approximately 100%.

3.7. ANN analysis

In this study, experimental results for the sorption of MB molecules from water-soluble solutions by AC/Fe_3O_4 NCs were modelled using the ANN method. The training procedure was accomplished by employing the standard BP algorithm as the optimization process. The ANN was created using the Levenberg-Marquardt (LM), Bayesian regularization (BR) and Scale Conjugated Gradient (SCG) algorithms (Figs. 13–15) to assess their extrapolative capacity. The Tang sigmoid (tansig) function was chosen as a stimulation function in this study, utilizing a data division ratio of 70:15:15. From the software generated “All” R^2 values of LM (0.9961) was the highest followed by BR (0.9911) and SCG (0.9541) (Figs. 13–15). BR script performance did not require validation as observed in Fig. 14, which was ascribed to pre-set net trainParam.max. fail function that program validation removal. Computational processes by the BR algorithm guarantee variation to noisy data sets by performing a reducing procedure employing an adjusted number of factors using a

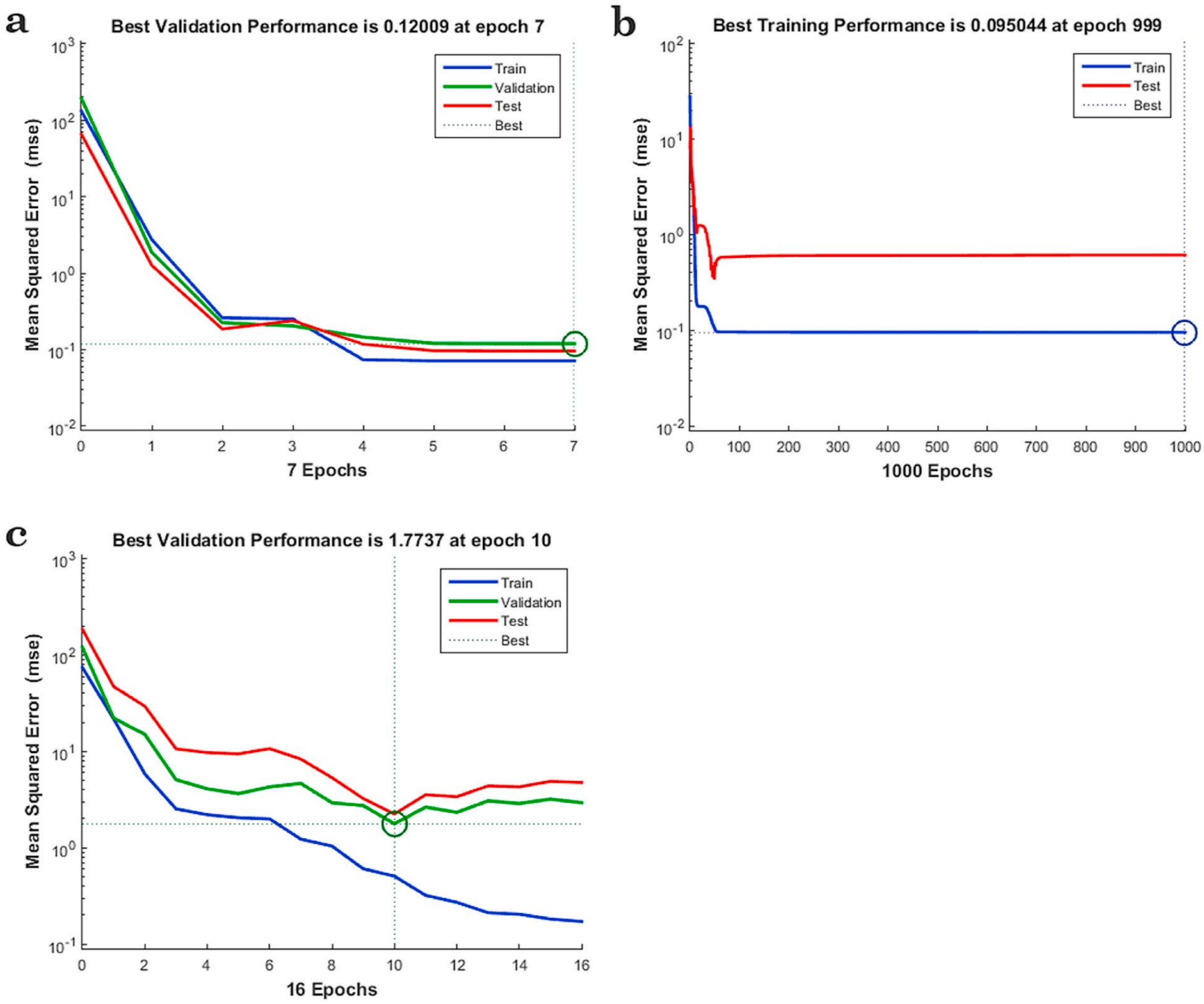

Fig. 17. The plot of MSE against the number of epochs in the hidden layer for (a) LM, (b) BR and (c) SCG.

statistical penalty term as depicted by Equation (16). Accurate BR bias created during regularization by the minimization procedure generates a less diverged data output.

$$F = \beta E_D(D / w, M) + \alpha E_w(w/M) \quad 16$$

E_D, D, β, and α, $\alpha E_w(w/M)$ signify the mean sum of squares active in decreasing overfitting, input-target training data, are the predicted hyper-parameters in the decay rate term and the decaying rate term (Makomere et al., 2023). The acquired ANN models show an excellent association from the training data for the optimized structures as shown in Figs. 13–15a. While it did not function reasonably well in the validation and testing, owing to scattered data points (Figs. 13–15b-c). Generally, the models functioned reasonably well for the sorption experimental data set as shown in Figs. 13–15d in the order of LM > BR > SCG.

3 inputs (pH, sorbent dosage, and MB concentrations) were specified in the system, and the neuron number in the hidden layer was determined to be 7. Results from individual tools training were attained when optimum interactions were achieved, where LM, BR and SCG training were inactivated at optimum 7, 1000 and 15 epochs simulations. There was no substantial change observed in the technique performance after simulating above these epochs (Fig. 16).

From Table 5, the generated functions and hidden node layout interpretation are based on the performance of R^2 and MSE as well as RMSE. The most efficient network model is the one with the superior R^2 as well as the lowest MSE and RMSE values. The sigmoid function (tansig) shows response relationships that are closer to the given values. The 3-7-1 architecture is exceptional to other network designs for LM, BR, and SCG training tools. The 7 hidden cells ideally enhance the precision, with which the system interprets the indistinct data. Therefore, the remaining layer is changed into a linear function and since the output created is also linear, the correlation between the data is impacted (Makomere et al., 2023). Based on the generated data, LM outperformed BR and SCG in describing the accuracy of MB sorption to the NCs based on the results presented in Table 5 owing to the highest R^2 in the training and validation and lowest MSE and RMSE values obtained in the training, validation, and testing. While BR outperformed LM and SCG in the testing based on the R^2 value obtained. According to Banza et al. (2023), an R^2 value that is greater than 0.8 established a satisfactory correlation between the predicted and experimental results (Banza et al., 2023b).

As observed in Fig. 17, the training processes were stopped after 7, 999 and 10 epochs for LM, BR, and SCG. As observed from this figure, the validation test was not executed for the BR coding approach, but in LM and SCG algorithms. This was ascribed to LM and SCG tools not making use of Equation (16) for generalization, as validation tests are necessary for verifying errors arising in the weights during the training procedure (Makomere et al., 2023).

The network was assessed by comparing its experimental values employing an independent data set (test data) with the predicted values obtained from the weight and bias values from ANN. The plots of the predicted data against the experimental data are shown in Fig. 18. It was

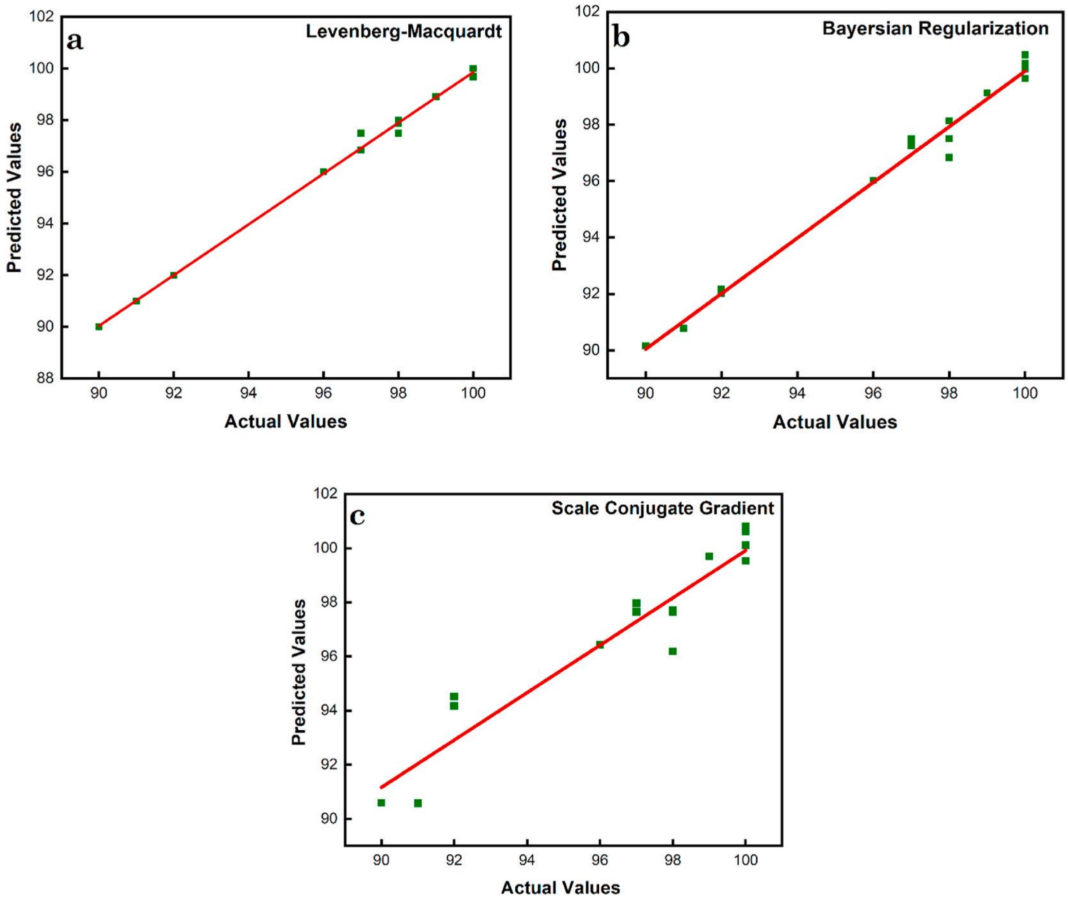

Fig. 18. Comparative study of the plot of the predictive data set of (a) LM, (b) BR and (c) SCR against the experimental data set.

Table 6
Comparative errors associated with the plots of the predictive data against the actual data for LM, BR and SCG.

Error Function	LM	BR	SCG
R^2	0.9922	0.9823	0.9103
Adjusted R^2	0.9918	0.9814	0.9053
RSS	1.4475	3.3383	14.4080
Pearson (r)	0.9961	0.9911	0.9541
MSE	0.1883	0.3026	1.1369
RMSE	0.4340	0.5501	1.0663

noticed that all the points in the plots were well distributed along the trendline of the scattered plots. R^2 values were determined for individual plots of predicted data against the actual data for LM, BR and SCG algorithms were 0.9922, 0.9823 and 0.9103, which showed the reliability of each model, with LM having the highest R^2 value and showed a better generalization performance. A satisfactory correlation was established between the actual and predicted data as R^2 values were > 0.8 for algorithms. The adjusted-R^2 values in Table 6 showed that the adjusted R^2 value was the highest followed by BR and SCG. The predicted R^2 value for LM, BR and SCG algorithms were in a realistic pact with the adjusted R^2 value for LM, BR and SCG algorithms and the difference between the predicted and adjusted R^2 values were 0.0004, 0.0009 and 0.005, which validates decent certainty of the model (difference should be < 0.2) (Banza et al., 2023a; Alipour et al., 2022). The MSE, RMSE and RSS errors using LM, BR and SCG algorithms were 0.1883, 0.3020 and 1.1369, 0.4340, 0.5501 and 1.0663, 1.4475, 3.3383 and 14.4080. The lowest obtained values using these algorithms were in the order of LM > BR > SCG. From these results, it was obvious that the LM algorithm fitted well with the data sets. From the data reported in Tables 6 and it was shown that there was a positive association between the predicted and experimental values for all algorithms. A comparison of the predicted and experimental removal efficiency is depicted in Table 2. It shows that the experimental removal efficiency values were close to that of the predicted % removal efficiency using the different algorithms, with LM being most comparative to the experimental removal efficiency. The ANN model was confirmed to be an acceptable interpolation tool that best predicted the sorption of MB dye molecules to AC/Fe_3O_4 NCs was the LM algorithm.

3.8. Isotherm models

A critical aspect of any scientific research is the modelling process. The sorption isotherm research offers an understanding of the nature of the sorbate-sorbent interaction (Hashem et al., 2022). The sorption equilibrium isotherm describes the equilibrium interaction between the sorbed ions in a water-soluble solution at a particular temperature (Singh and Balomajumder, 2017). To link the isotherm equilibrium data, three isotherm models were explored utilizing the linear form (LFm) and NL form (NLFm) of the Langmuir (LNRM), FRHM and Temkin (TENM) models, which were fitted using Originlab 9 software.

The LNRM was mainly intended to explain the gas-solid phase sorption and is mainly utilized to compute and compare the different sorbent sorptive capacities. It also accounts for surface coverage by assessing the comparative desorption and sorption rate (energetic equilibrium). Sorption is comparative to the segment of the sorbent surface that is open while desorption is relative to the part of the sorbent surface that is covered. While the FRHM is appropriate to the sorption process that takes place on heterogeneous surfaces. This model gives an illustration which is used to describe the heterogeneity of a surface and

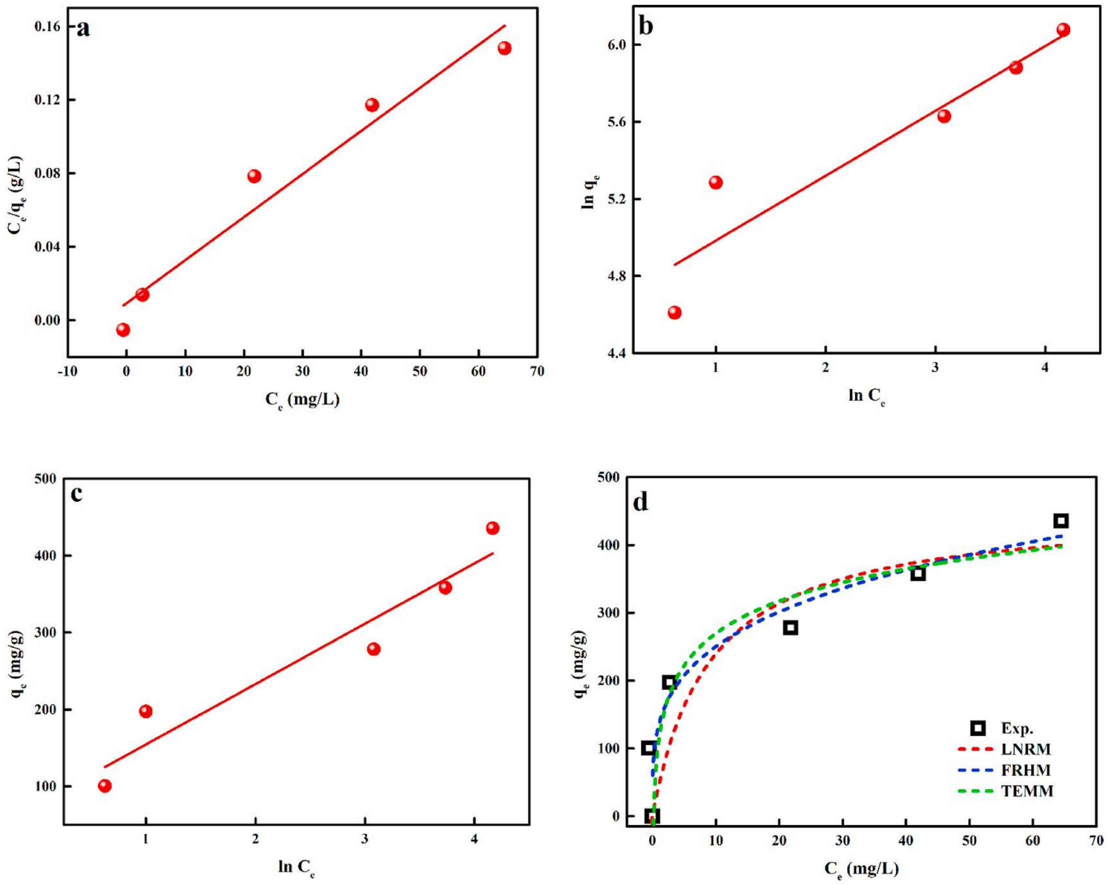

Fig. 19. Linear plots of (a) LNRM, (b) FRHM, (c) TENM and (d) NLF of isotherm models (experimental conditions: initial concentrations-100-500 mg.L^{-1}, dosage-50 mg, interaction time-60 min and pH-10).

Table 7
Determined parameters from the LF of isotherm models.

LNRM			FRHM			TENM		
LF								
K_L (L.mg^{-1})	q_m(cal) (mg.g^{-1})	R^2	K_F ((mg.g^{-1})(L/mg)$^{1/n}$)	n	R^2	K_T (L.mg^{-1})	B (J/mol)	R^2
0.2522	427.3504	0.94197	104.3990	2.9741	0.8437	2.6385	0.0128	0.8999

the exponential dissemination of active sites and their energies (Ayawei et al., 2017; Sahoo and Prelot, 2020). The TENM comprises of the sorption heat in layers of molecules which reduces linearly owing to the sorbent sorbate interactions and such sorption is distinguished by the bonding energies' equal distribution. This model was expressed in the case of the gases on solids sorption and liquid phase transportation and gives access to the sorption energy modification which exemplifies how the pollutant molecules are maintained on the sorbent surface (Togue Kamga, 2019). The NLF models of the isotherm models are depicted by Equations (17)–(19).

$$q_e = \frac{q_m K_L C_e}{1 + K_L C_e} \quad (17)$$

$$q_e = K_F C_e^{1/n} \quad (18)$$

$$q_e = \frac{RT}{B} \ln(K_T C_e) \quad (19)$$

K_L, K_F, n, B and K_T represent LNRM binding energy, FRHM constant symbolizing capacity, FRHM exponent, TENM constant relating to sorption heat variation and optimum binding energy (Lee et al., 2021).

The results of the fittings of the various models are shown in Fig. 19a–c. While results of the determined parameters from the linear fitting (LF) and NLF with their equivalent R^2, X^2 and RSS values are shown in Tables 7 and 8. It was noticed from Table 8, that the FRHM superlative defined the sorption of MB to AC/Fe_3O_4 NCs due to their elevated R^2 values and lowest X^2 and RSS values obtained. The optimum sorption capacity determined according to the LNRM was 455.0153 mg g^{-1}. Also, the n value determined from the FRHM was 3.7180, which was greater than 1 and indicative of the appropriateness of AC/Fe_3O_4 NCs for MB dye sequestration. The calculated and experimental data from the FRHM were very close. The sorption capacity of different NCs utilized for the confiscation of MB dye is reported in Table 9 and it was noticed that the sorption capacity of the NCs employed in this study was comparable high against other NCs used for the confiscation of MB dye. Multilayer sorption due to heterogeneous site distribution with various sorption energies was responsible for the MB dye molecule's sorption to AC/Fe_3O_4 NCs (Al-Ghouti and Da'ana, 2020). Table 9 illustrates the comparison of the optimum sorption capacities of AC/Fe_3O_4 NCs and other sorbents employed for the confiscation of MB. A direct comparison of the sorption performance is challenging owing to various experimental conditions, but this is a useful benchmark for physically

Table 8
Determined parameters from the NLF of isotherm models.

LNRM					FRHM					TENM				
NLF														
K_L ($L.mg^{-1}$)	q_m(cal) ($mg.g^{-1}$)	R^2	X^2	RSS	K_F (($mg.g^{-1}$)(L/mg)$^{1/n}$)	n	R^2	X^2	RSS	K_T ($L.mg^{-1}$)	B (J/mol)	R^2	X^2	RSS
0.1113	455.0153	0.7283	7156.3930	28625.5719	134.7138	3.7180	0.8854	3017.7427	12070.9710	5.1241	68.5307	0.8675	3488.9170	13955.6678

Table 9
Comparison of the optimum sorption capacities of various nanosorbents for MB dye removal.

Nanosorbents	q_m ($mg.g^{-1}$)	References
AC/Fe_3O_4 NCs	455	This study.
ZnO-Chitosan NCs	98	Zango et al. (2020)
Anisomeles malabarica silver NPs	97	Prabhahar et al. (2022)
Bio-modified MNPs	294	Das et al. (2022)
AC derived from mixed orange and watermelon rind activated with $ZnCl_2$	201	Hanafi et al. (2022)
$ZnFe_2O_4$	257	Zhao et al. (2022).
Functionalized biomass carbon-based sorbent	250	Fan et al. (2022)
Montmorillonite/$NiFe_2O_4$@amine-functionalized chitosan NCs	137	Gomaa et al. (2022)
Nanoparticles-doped AC	157	Obayomi et al. (2022)
Fe_3O_4	72	Bassim et al. (2022)
MNCs by Cordia Africana	30	Zenebe et al. (2021)

assessing materials potential (Eldeeb et al., 2022; Elwakeel et al., 2017).

3.9. Kinetic study

In the sorption process, contact time is central due to it permitting the diffusion and adhesion of sorbate molecules to transpire (Kurniawati et al., 2021). To assess the influence of contact-time on the confiscation of MB dye to AC/Fe_3O_4 NCs, this study was implemented in a varying time of 5–60 min at pH 10. As noticed in Fig. 20a, there was a fast improvement in the % of MB dye sorbed to the AC/Fe_3O_4 NCs as the contact time of the process was enhanced and the optimum contact time for MB dye to be confiscated was observed at 15 min, which was ascribed to the binding process between the dye molecules and the available active sorption sites on the NCs surface. Further increase in the contact time of the sorption process resulted in no considerable removal being observed (slow sorption process), owing to the active sites on the NCs saturation (Kuang et al., 2020; Thabede et al., 2020). The time-dependence of the sorption system is interpreted by the kinetic study (Hashem et al., 2022). These models also control the sorption rate, which defines the requisite time for the process of sorption to attain equilibrium. These models can also give knowledge about the pathways for sorption and the possible mechanisms involved. To comprehend the meticulous sorption process attributes, the different kinetic models employed in this study were the pseudo-first-order-model (PFOM), PSOM, and intraparticle diffusion model (INDM) employing the linear and the NL model's equations (Sahoo and Prelot, 2020). The NLNF models of the kinetic models are represented by Equations (20)–(22).

$$q_t = q_e\left(1 - e^{-k_1 t}\right) \quad 20$$

$$q_t = \frac{q_e^2 k_2 t}{1 + q_e k_2 t} \quad 21$$

$$q_t = k_{INT} t^{0.5} + C \quad 22$$

k_1, k_2, k_{IND} and C represent the PFOM, and PSOM rate constants in (1/min) and (g/mg.min), INDM rate constant (g/mg.min) and boundary layer outcome or surface sorption (Ofomaja et al., 2020).

Comparison of the determined coefficient of regression (R^2) parameter from the LF of the PFOM, PSOM and INDM (Fig. 20b–d), it was noted that the PSOM with R^2 = 0.9999 and 1.000 values superlative represented the sorption of 100 and 200 $mg.L^{-1}$ concentrations of MB dye molecules to the AC/Fe_3O_4 NCs (Table 10). Employing the NLF to the various kinetic models, the kinetic model that most excellently explained the sorption process of MB to AC/Fe_3O_4 NCs was determined

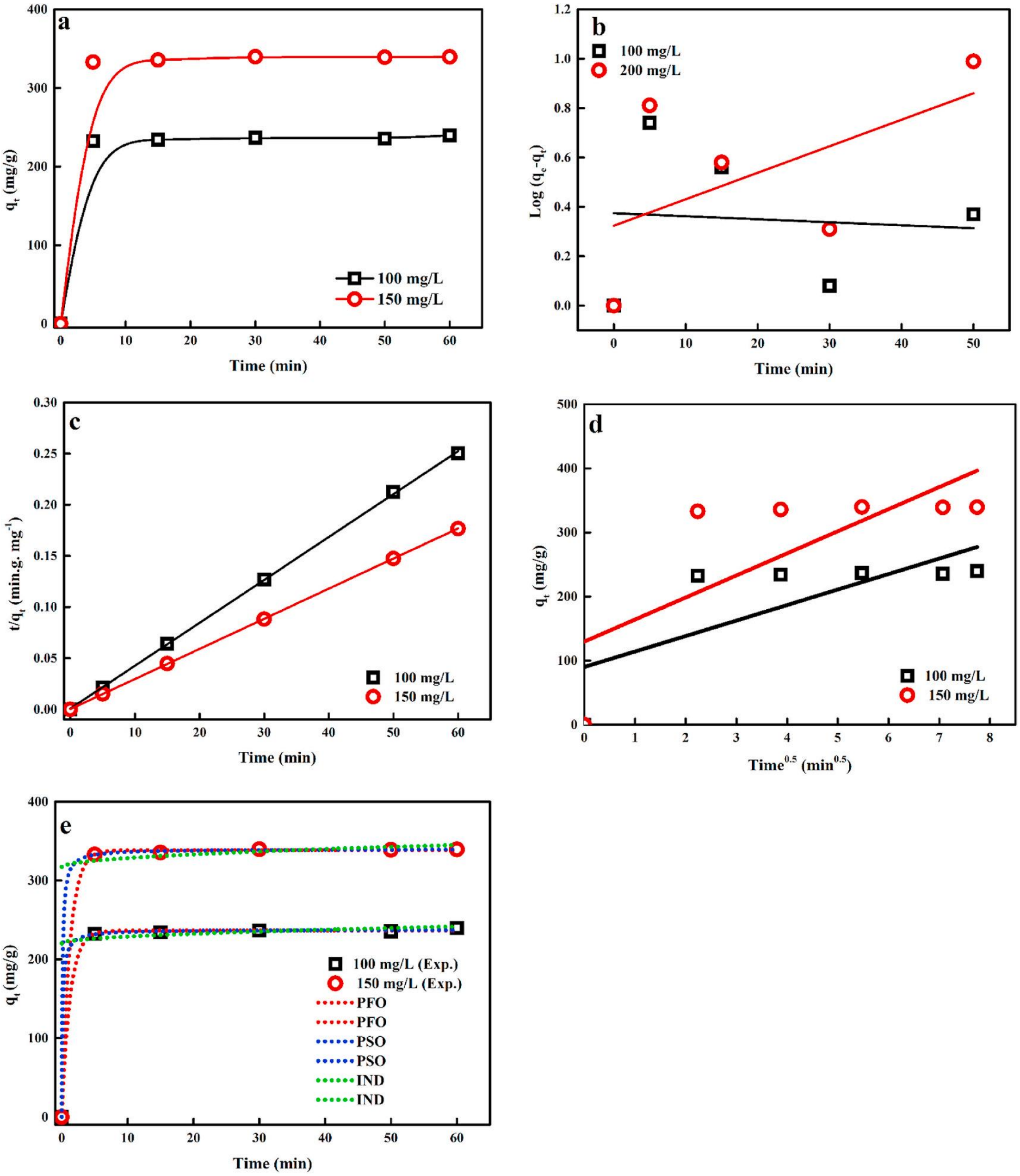

Fig. 20. Linear plots of (a) impact of time on the elimination of MB elimination (b) PFOM, (c) PSOM, (d) INDM and (e) NLF of kinetic models (experimental conditions: initial concentrations-100 and 150 $mg.L^{-1}$, dosage-20 mg, interaction time-5-60 min and pH-10).

Table 10
Determined parameters from the LF of kinetic models.

Conc. ($mg.L^{-1}$)	PFOM			PSOM			INDM		
	LF								
	k_1 (min^{-1})	q_e(cal) ($mg.g^{-1}$)	R^2	k_2 ($g/mg^{-1}.min^{-1}$)	q_e(cal) ($mg.g^{-1}$)	R^2	K_{IND}	C_t ($mg.L^{-1}$)	R^2
100	0.0012	1.4537	−0.3250	0.0250	238.6635	0.9998	24.16408	89.97801	0.44098
200	0.0107	1.3817	0.0745	0.0395	340.1361	1.0000	34.4370	129.56108	0.43465

by the maximum values of the (R^2) and lowest possible values of X^2 and RSS. A superior value of X^2 and RSS was indicative of a high-level bias between the calculated and experimental model values (Jasper et al., 2020; Benmessaoud et al., 2020). The ultimate model for the sorption of MB dye to AC/Fe_3O_4 NCs was well-thought-out using the NLF of the kinetic models and the determined parameters from the NLF of all models showed that the PSOM superlative defined the sorption process of MB dye molecules which closely trailed by the PFOM and the INDM, with the calculated parameters of R^2, X^2 and RSS established to be 0.9997/0.9999, 2.8255/1.1492 and 11.3020/4.5966 for PSOM,

Table 11
Determined parameters from the NLF of kinetic models.

Conc. ($mg.L^{-1}$)	PFOM NLF					PSOM					INDM				
	k_1 (min^{-1})	q_e(cal) ($mg.g^{-1}$)	R^2	X^2	RSS	k_2 ($g/mg^{-1}.min^{-1}$)	q_e(cal) ($mg.g^{-1}$)	R^2	X^2	RSS	K_{IND}	C_t ($mg.L^{-1}$)	R^2	X^2	RSS
100	0.8076	236.4099	0.9996	4.1184	16.4735	0.0342	237.5146	0.9997	2.8255	11.3020	2.7546	220.1477	0.1829	113.0746	112848.4819
200	0.8241	338.4225	0.9999	2.7225	10.8898	0.0272	339.7674	0.9999	1.1492	4.5966	3.6123	317.0581	0.1676	216.1002	215667.9634

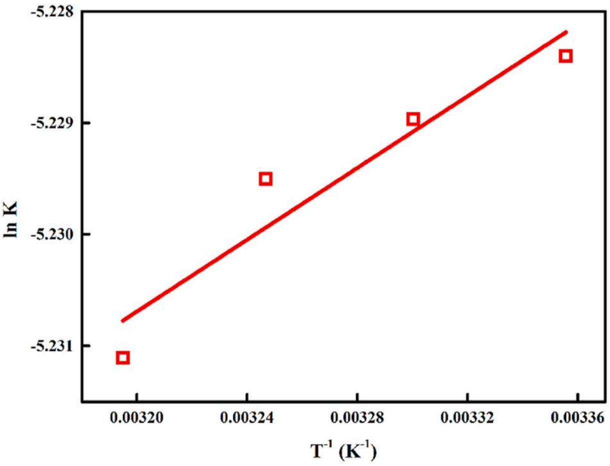

Fig. 21. Vant's Hoff plot of ln K vs. T^{-1} (experimental conditions: initial concentrations-100 $mg.L^{-1}$, dosage-50 mg, interaction time-30 min, temperature-298-313 K and pH-10).

Table 12
Determined thermodynamic parameters of MB elimination.

Dye	Temperature (K)	Δ**G°** (kJ/mol)	Δ**H**° (kJ/mol)	Δ**S**° (J/mol.K)
MB	298	13.22	0.13	−43.92
	303	13.44		
	308	13.66		
	313	13.88		

0.9996/0.9999, 4.1184/2.7225 and 16.4735/10.8898 for PFOM and 0.1829/0.1676, 113.0746/216.1002and 112848.4819/215667.9634 for INDM) model for 100 and 200 $mg.L^{-1}$ concentrations of MB dye (Table 11). The values of calculated q_e ($mg.g^{-1}$) of the PSOM for the LF and NLF were relatively close to the experimental values. The plots of the INDM of the sorption process of MB dye were not rate-controlling and diffused through the liquid film of the AC/Fe_3O_4 NCs, as the straight line did not pass via the origin of the plot and the R^2 values were comparatively poor. Hence the sorption of MB dye to AC/Fe_3O_4 NCs was centred on the rate-limiting step of chemical sorption or chemisorption which further collaborates with the findings from the studies of (Zhao et al., 2022; Fan et al., 2022; Ratnam et al., 2022). The INDM was employed to ascertain the level-limiting step of the sorption process and if the regression of the linear plot of this model passes via the origin, then according to this model sorption process is controlled by INDM (Miyah et al., 2018).

3.10. Thermodynamics study

Through the thermodynamic parameters (the Gibbs free energy ($\Delta G°$), the enthalpy ($\Delta H°$) and the entropy ($\Delta S°$)), an understanding of the sorption mechanism can be assessed. The equilibrium constant (K) is considered by extrapolating the Van't Hoff plot of ln (q_e/C_e) against T^{-1} to zero (Fig. 21) and the values of $\Delta H°$ and $\Delta S°$ are found from the slope and intercept of equation (20). The thermodynamics parameters are assessed using Equations (23)–(25).

$$\Delta G^\circ = -(RT \ln K) \tag{23}$$

$$\Delta G^\circ = \Delta H^\circ - T\Delta S^\circ \tag{24}$$

$$ln\ K = \frac{\Delta H^\circ}{R} \times \frac{1}{T} - \frac{\Delta S^\circ}{R} \tag{25}$$

T and R are the absolute temperature in Kelvin (K) and the universal gas constant (J/mol/K) (Abbas, 2022; Kheddo et al., 2020). According to

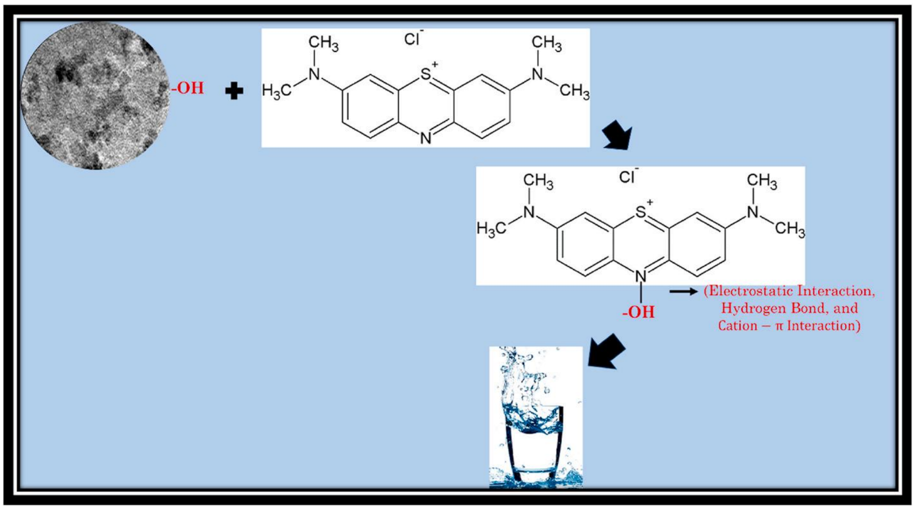

Fig. 22. Possible mechanism of MB sorption to AC/Fe_3O_4 NCs.

the parameters determined and which is reported in Table 12, the positive values of ΔG° and ΔH° were indicative of a non-spontaneous and endothermic MB sorption to the NCs. The determined values of ΔG° were noticed to improve with increasing temperature applied to the system and its values were between 0 and 20 kJ/mol, which was suggestive of a physisorption process. The positive values of ΔH° and ΔG°, which increase with intensifying temperature presented a sorption process that was favourable at elevated temperatures. This was ascribed to the sorbate mobility and affinity increasing with an increase in temperature. The negative value of ΔS° determined was suggestive of to a lesser extent disorder in the sorption of MB to the NCs and its value was less than 1 (0.0439 kJ/mol.K), which was suggestive of a reversible reaction (Table 12) (Amin et al., 2017; Tcheka et al., 2022; Potgieter et al., 2021; Abbas, 2022; Kheddo et al., 2020; Onu et al., 2022).

3.11. Mechanism of MB sorption

To completely comprehend the mechanism of MB adsorption to AC/Fe_3O_4 NCs, a precise understanding of the sorption mechanism is important. Depending on the surface and textural properties of the sorbent as well as how the adsorbate diffuses towards it, a mix of chemisorption and physisorption drives the sorption process of MB dye (Kangmennaa et al., 2024). As evident from FTIR analysis, cationic MB dye molecules were confiscated to the negatively charged oxygenated functional groups such as C–O and $^-$OH present on the surface of the synthesized AC/Fe_3O_4 NCs in the water-soluble medium via ion exchange. These groups have a sturdy capacity to draw species with a converse charge and repel those with an identical charge. Hence, cationic MB dye was sturdily magnetized from the solution to the AC/Fe_3O_4 NCs. Additionally, the dye removal comprises of the electrostatic attraction, hydrogen bonding, and cation – π interaction with the aromatic ring of the dye, which is critical in the mechanism as shown in Fig. 22. An increase in solution pH led to increased removal of MB to AC/Fe_3O_4 NCs owing to the electrostatic attraction between cationic MB dye and deprotonated sites on the sorbent ($^-$OH). Also, the existence of a hydrogen bond between $^-$OH of the AC/Fe_3O_4 NCs and nitrogen of MB was ascribed to MB sorption. MB being a planar molecule with an aromatic ring, the p-electrons existing in the MB molecular structure will couple with AC/Fe_3O_4 NCs to form cation – π interaction, hence, promoting MB dye molecules sorption to the surface of AC/Fe_3O_4 NCs (Kangmennaa et al., 2024; Elkholy et al., 2023; Hu et al., 2018; El-Nemr et al., 2022; Salazar-Rabago et al., 2017; Li et al., 2020; Dehbi et al., 2024)

4. Conclusion

In this study, AC/Fe_3O_4 NCs were fabricated and employed for effective MB dye sequestration. Optimization was implemented using the CCD-based RSM technique to save cost and time and attain the least error response. According to the CCD-based RSM technique, the quadratic model was practically accurate in explaining the sorption of MB dye to AC/Fe_3O_4 NCs. The optimal conditions for eliminating MB dye according to the DF were pH-9.6, sorbent dosage-73 mg. initial concentration-172 mg.L^{-1} and removal efficiency of 100%. Also, sorbent dosage and initial concentration are substantial terms with a P-value <0.05 in the model and had central control over the MB dye sorption process. Based on the NLF of the kinetic and isotherm models, the sorption of MB dye to AC/Fe_3O_4 NCs was perfectly classified using the PSOM and FRHM. The determined optimal sorption capacity was 455 mg g^{-1}. Thermodynamically, MB dye sorption to AC/Fe_3O_4 NCs was found to be non-spontaneous and endothermic in nature. Thus, AC/Fe_3O_4 NCs were a capable sorbent for the sequestration of MB dye and a possible process scale-up information was provided by the RSM. The ANN approach as an attractive choice for modelling complex systems like wastewater treatment procedures owing to it being an effective, generalizable, and simple tool was explored in this study. The % of MB dye molecules removed from water-soluble solutions was projected employing the ANN model using experimental data generated. This was achieved using the 3-7-1 NN architecture and with pH, sorbent dosage and initial dye concentrations serving as the input data for the ANN system. Based on the three training algorithms employed in this study, the LM was found to better predict the sorption process based on the determined high R^2 (0.9922), and low RMSE (0.3020) and MSE (0.1883) values. Comparison between the modelled experimental and predicted data showed significantly identical predicted output to the experimental data with the LM algorithm having a high R^2, which showed the applicability of the NN model for defining the sorption of MB to AC/Fe_3O_4 NCs with a practical precision.

CRediT authorship contribution statement

Uyiosa Osagie Aigbe: Conceptualization, Data curation, Formal analysis, Funding acquisition, Methodology, Software, Validation, Writing – original draft, Writing – review & editing. **Thabang Calvin Lebepe:** Formal analysis, Investigation. **Oluwatobi Samuel Oluwafemi:** Supervision, Writing – review & editing. **Otolorin Adelaja Osibote:** Funding acquisition, Resources, Supervision, Writing – review & editing.

Declaration of competing interest

The authors declare that they have no known competing financial interests or personal relationships that could have appeared to influence the work reported in this paper.

Data availability

Data will be made available on request.

Acknowledgement

The authors are grateful to the Cape Peninsula University of Technology and the National Research Foundation for the funding of this project and to the Centre for Nanomaterials and Science Research, University of Johannesburg, Johannesburg, South Africa; Department of Chemical Sciences (Formerly Applied Chemistry) for the use of their facility and equipment for this research.

References

Abbas, M., 2022. Removal of methylene blue pollutant from the textile industry by adsorption onto Zeolithe: kinetic and thermodynamic study. Journal of Engineered Fibers and Fabrics 17, 1558925021993692.
Abdel-Ghani, N., El-Chaghaby, G., Rawash, E., Lima, E., 2019. Magnetic activated carbon nanocomposite from Nigella sativa L. waste (MNSA) for the removal of Coomassie brilliant blue dye from aqueous solution: statistical design of experiments for optimization of the adsorption conditions. J. Adv. Res. 17, 55–63.
Abussaud, B., Asmaly, H., Saleh, T., Gupta, V., Atieh, M., 2016. Sorption of phenol from waters on activated carbon impregnated with iron oxide, aluminum oxide and titanium oxide. J. Mol. Liq. 213, 351–359.
Agbaogun, B., Olu-Owolabi, B., Buddenbaum, H., Fischer, K., 2023. Adaptive neuro-fuzzy inference system (ANFIS) and multiple linear regression (MLR) modelling of Cu, Cd, and Pb adsorption onto tropical soils. Environ. Sci. Pollut. Control Ser. 30 (11), 31085–31101.
Ahmad, Z., Yao, L., Lian, Q., Islam, F., Zappi, M., Gang, D., 2020. The use of artificial neural network (ANN) for modeling adsorption of sunset yellow onto neodymium modified ordered mesoporous carbon. Chemosphere 256, 127081.
Ahmed, M., Ahmaruzzaman, M., 2015. A facile synthesis of Fe3O4–charcoal composite for the sorption of a hazardous dye from aquatic environment. J. Environ. Manag. 163, 163–173.
Aigbe, U., Khenfouch, M., Ho, W., Maity, A., Vallabhapurapu, V., Hemmaragala, N., 2018. Congo red dye removal under the influence of rotating magnetic field by polypyrrole magnetic nanocomposite. Desalination Water Treat. 131, 328–342.
Aigbe, U., Ukhurebor, K., Onyancha, R., Osibote, O., Darmokoesoemo, H., Kusuma, H., 2021. Fly ash-based adsorbent for adsorption of heavy metals and dyes from aqueous solution: a review. J. Mater. Res. Technol. 14, 2751–2774.
Aigbe, U., Ukhurebor, K., Onyancha, R., Okundaye, B., Aigbe, E., Obodo, K., Omamoke, E., Noto, L., Osibote, A., Atagana, H., 2023a. Activated biosorbents for the removal of metals from aqueous solutions. In: Adsorption Applications for Environmental Sustainability. IOP Publishing, Bristol, UK, pp. 3–11.
Aigbe, U., Maluleke, R., Lebepe, T., Oluwafemi, O., Osibote, O., 2023b. Rhodamine 6G dye adsorption using magnetic nanoparticles synthesized with the support of Vernonia Amygdalina leaf extract (bitter leaf). J. Inorg. Organomet. Polym. Mater. 1–20.
Al-Ghouti, M., Da'ana, D., 2020. Guidelines for the use and interpretation of adsorption isotherm models: a review. J. Hazard Mater. 393, 122383.
Al-Zawahreh, K., Barral, M., Al-Degs, Y., Paradelo, R., 2021. Comparison of the sorption capacity of basic, acid, direct and reactive dyes by compost in batch conditions. J. Environ. Manag. 294, 113005.
Ali, R., Aslam, Z., Shawabkeh, R., Asghar, A., Hussein, I., 2020. BET, FTIR, and Raman characterizations of activated carbon from waste oil fly ash. Turk. J. Chem. 44 (2), 279–295.
Alipour, A., Zarrinabadi, S., Azimi, A., Mirzaei, M., 2022. Effective removal of heavy metal using cellulose nanocomposite adsorbents: response surface methodology. Iranian (Iranica) Journal of Energy & Environment 13 (3), 258–272.
Altintig, E., Özcelik, T., Aydemir, Z., Bozdag, D., Kilic, E., Yilmaz Yalciner, A., 2023. Modeling of methylene blue removal on Fe3O4 modified activated carbon with artificial neural network (ANN). Int. J. Phytoremediation 1–19.
Amin, M., Alazba, A., Shafiq, M., 2017. Nonspontaneous and multilayer adsorption of malachite green dye by Acacia nilotica waste with dominance of physisorption. Water Sci. Technol. 76 (7), 1805–1815.
Amor, N., Noman, M., Petru, M., 2021. Prediction of methylene blue removal by nano TiO2 using deep neural network. Polymers 13 (18), 3104.
Ararem, A., Bouzidi, A., Mohamedi, B., Bouras, O., 2014. Modeling of fixed-bed adsorption of Cs+ and Sr 2+ onto clay–iron oxide composite using artificial neural network and constant–pattern wave approach. J. Radioanal. Nucl. Chem. 301, 881–887.
Archana, S., Jayanna, B., Ananda, A., Ananth, M., Ali, A., Muralidhara, H., Kumar, K., 2022. Numerical investigations of response surface methodology for organic dye adsorption onto Mg-Al LDH-GO Nano Hybrid: an optimization, kinetics and isothermal studies. J. Indian Chem. Soc. 99 (1), 100249.
Ayawei, N., Ebelegi, A., Wankasi, D., 2017. Modelling and interpretation of adsorption isotherms. J. Chem. 2017.
Bankole, O., Osuntokun, O., Adeola, A., Owoeye, A., 2020. Ocimum gratissimum capped sulfur nanoparticles and antibacterial efficacy against multidrug-resistant microbes. Asian J. Res. Biochem 7, 84–95.
Banza, M., Seodigeng, T., Rutto, H., 2023a. Comparison study of ANFIS, ANN, and RSM and mechanistic modeling for chromium (VI) removal using modified cellulose nanocrystals–sodium alginate (CNC–Alg). Arabian J. Sci. Eng. 1–19.
Banza, M., Rutto, H., Seodigeng, T., 2023b. Application of artificial neural network and shrinking core model for copper (Ii) and lead (Ii) leaching from contaminated soil using ethylenediaminetetraacetic acid. Soil Sediment Contam.: Int. J. 1–21.
Bassim, S., Mageed, A., AbdulRazak, A., Majdi, H., 2022. Green synthesis of Fe3O4 nanoparticles and its applications in wastewater treatment. INORGA 10 (12), 260.
Benmessaoud, A., Nibou, D., Mekatel, E., Amokrane, S., 2020. A comparative study of the linear and non-linear methods for determination of the optimum equilibrium isotherm for adsorption of Pb2+ ions onto Algerian treated clay. Iran. J. Chem. Chem. Eng. (Int. Engl. Ed.) 9 (4), 153–171.
Blessing, A., Arinzechukwu, C., Emeka, O., 2017. Protecting mild steel from acid corrosion using extract from Ocimum gratissimum leaves. Int. Lett. Chem. Phys. Astron. 73, 9–21.
Buhani, D.J., Fajriyah, N., Rilyanti, M., Suharso, S., Elwakeel, K., 2023a. Modification of non-activated carbon from rubber fruit shells with 3-(aminopropyl)-triethoxysilane and its adsorption study on coomassie brilliant blue and methylene blue in solution. Water, Air, Soil Pollut. 234 (9), 578.
Buhani, S.R.M., Antika, F., Lestari, L., Sumadi, A.M., Elwakeel, K., 2023b. Functionalization of carbon from rubber fruit shells (Hevea brasiliensis) with silane agents and its application to the adsorption of bi-component mixtures of methylene blue and crystal violet. Environ. Sci. Pollut. Control Ser. 1–14.
Das, C., Singh, S., Bhakta, S., Mishra, P., Biswas, G., 2022. Bio-modified magnetic nanoparticles with Terminalia arjuna bark extract for the removal of methylene blue and lead (II) from simulated wastewater. Chemosphere 291, 132673.
Dehbi, A., Dehmani, Y., Franco, D., Omari, H., Georgin, J., Brahmi, Y., Elazhari, K., Messaoudi, M., Aadnan, I., Lamhasni, T., Alrashdi, A., 2024. A statistical physics approach to understanding the adsorption of methylene blue onto cobalt oxide nanoparticles. Molecules 29 (2), 412.
Dey, A., Dey, A., 2021. Selection of optimal processing condition during removal of methylene blue dye using treated Betel Nut fibre implementing desirability based RSM approach. In: Response Surface Methodology in Engineering Science. IntechOpen, London, UK.
Drummer, S., Madzimbamuto, T., Chowdhury, M., 2021. Green synthesis of transition-metal nanoparticles and their oxides: a review. Materials 14 (11), 2700.
Dubey, S., Gusain, D., Sharma, Y., 2016. Kinetic and isotherm parameter determination for the removal of chromium from aqueous solutions by nanoalumina, a nanoadsorbent. J. Mol. Liq. 219, 1–8.
Eddy, N., Ibok, U., Garg, R., Garg, R., Iqbal, A., Amin, M., Mustafa, F., Egilmez, M., Galal, A., 2022. A brief review on fruit and vegetable extracts as corrosion inhibitors in acidic environments. Molecules 27 (9), 2991.
El-Nemr, M., Aigbe, U., Ukhurebor, K., Onyancha, R., El Nemr, A., Ragab, S., Osibote, O., Hassaan, M., 2022. Adsorption of Cr6+ ion using activated Pisum sativum peels-triethylenetetramine. Environ. Sci. Pollut. Control Ser. 29 (60), 91036–91060.
Eldeeb, T., Aigbe, U., Ukhurebor, K., Onyancha, R., El-Nemr, M., Hassaan, M., Ragab, S., Osibote, O., El Nemr, A., 2022. Adsorption of methylene blue (MB) dye on ozone, purified and sonicated sawdust biochars. Biomass Conversion and Biorefinery 1–23.
Eleryan, A., Hassaan, M., Aigbe, U., Ukhurebor, K., Onyancha, R., El-Nemr, M., Ragab, S., Hossain, I., El Nemr, A., 2023. Kinetic and isotherm studies of Acid Orange 7 dye absorption using sulphonated Mandarin biochar treated with TETA. Biomass Conversion and Biorefinery 1–12.
Elkholy, A., Yahia, M., Elnwawy, M., Gomaa, H., Elzaref, A., 2023. Synthesis of activated carbon composited with Egyptian black sand for enhanced adsorption performance toward methylene blue dye. Sci. Rep. 13 (1), 4209.
Elwakeel, K., El-Bindary, A., El-Sonbati, A., Hawas, A., 2016. Adsorption of toxic acidic dye from aqueous solution onto diethylenetriamine functionalized magnetic glycidyl methacrylate-N, N′-methylenebisacrylamide. RSC Adv. 6 (4), 3350–3361.
Elwakeel, K., El-Bindary, A., Kouta, E., 2017. Retention of copper, cadmium and lead from water by Na-Y-Zeolite confined in methyl methacrylate shell. J. Environ. Chem. Eng. 5 (4), 3698–3710.
Elwakeel, K., El-Bindary, A., Kouta, E., Guibal, E., 2018. Functionalization of polyacrylonitrile/Na-Y-zeolite composite with amidoxime groups for the sorption of Cu (II), Cd (II) and Pb (II) metal ions. Chem. Eng. J. 727–736.
Elwakeel, K., Shahat, A., Al-Bogami, A., Wijesiri, B., Goonetilleke, A., 2020. The synergistic effect of ultrasound power and magnetite incorporation on the sorption/desorption behavior of Cr (VI) and as (V) oxoanions in an aqueous system. J. Colloid Interface Sci. 569, 76–88.
Fan, X., Peng, L., Wang, X., Han, S., Yang, L., Wang, H., Hao, C., 2022. Efficient capture of lead ion and methylene blue by functionalized biomass carbon-based adsorbent for wastewater treatment. Ind. Crop. Prod. 183, 114966.
Geneti, S., Mekonnen, G., Murthy, H., Mohammed, E., Ravikumar, C., Gonfa, B., Sabir, F., 2022. Biogenic synthesis of magnetite nanoparticles using leaf extract of Thymus schimperi and their application for monocomponent removal of chromium and mercury ions from aqueous solution. J. Nanomater. 2022.
Ghoniem, M., Ali, F., Abdulkhair, B., Elamin, M., Alqahtani, A., Rahali, S., Ben Aissa, M., 2022. Highly selective removal of cationic dyes from wastewater by MgO nanorods. Nanomaterials 12 (6), 1023.

Gomaa, H., El-Monaem, A., Eman, M., Eltaweil, A., Omer, A., 2022. Efficient removal of noxious methylene blue and crystal violet dyes at neutral conditions by reusable montmorillonite/NiFe2O4@ amine-functionalized chitosan composite. Sci. Rep. 12 (1), 1–16.
Gupta, G., Sagar, P., Pandey, S., Srivastava, M., Singh, A., Singh, J., Srivastava, A., Srivastava, S., Srivastava, A., 2021. In situ fabrication of activated carbon from a bio-waste Desmostachya bipinnata for the improved supercapacitor performance. Nanoscale Res. Lett. 16 (1), 1–12.
Hajati, S., Ghaedi, M., Yaghoubi, S., 2015. Local, cheep and nontoxic activated carbon as efficient adsorbent for the simultaneous removal of cadmium ions and malachite green: optimization by surface response methodology. J. Ind. Eng. Chem. 21, 760–767.
Hamedi, A., Trotta, F., Borhani Zarandi, M., Zanetti, M., Caldera, F., Anceschi, A., Nateghi, M., 2019. In situ synthesis of MIL-100 (Fe) at the surface of Fe3O4@ AC as highly efficient dye adsorbing nanocomposite. Int. J. Mol. Sci. 20 (22), 5612.
Hanafi, N., Abdulhameed, A., Jawad, A., Alothman, Z., Yousef, T., Al Duaij, O., Alsaiari, N., 2022. Optimized removal process and tailored adsorption mechanism of crystal violet and methylene blue dyes by activated carbon derived from mixed orange peel and watermelon rind using microwave-induced ZnCl2 activation. Biomass Conversion and Biorefinery 1–13.
Hashem, A., Aniagor, C., Morsy, O., Abou-Okeil, A., Aly, A., 2022. Apricot seed shell: an agro-waste biosorbent for acid blue193 dye adsorption. Biomass Conversion and Biorefinery 1–14.
Hu, Z., Gao, Z., Liu, X., Yuan, Z., 2018. High-surface-area activated red mud for efficient removal of methylene blue from wastewater. Adsorpt. Sci. Technol. 36 (1–2), 62–79.
Hussein, A., Dannoun, E., Aziz, S., Brza, M., Abdulwahid, R., Hussen, S., Rostam, S., Mustafa, D., Muhammad, D., 2020. Steps toward the band gap identification in polystyrene based solid polymer nanocomposites integrated with tin titanate nanoparticles. Polymers 12 (10), 2320.
Igwegbe, C., Mohmmadi, L., Ahmadi, S., Rahdar, A., Khadkhodaiy, D., Dehghani, R., Rahdar, S., 2019. Modeling of adsorption of methylene blue dye on Ho-CaWO4 nanoparticles using response surface methodology (RSM) and artificial neural network (ANN) techniques. MethodsX 6, 1779–1797.
Ikimi, C., Abosede, O., 2022. Synthesis of copper oxide nanoparticles using Ocimum gratissimum (scent leaf). Asian Journal of Chemical Sciences 35–41.
Jasper, E., Ajibola, V., Onwuka, J., 2020. Nonlinear regression analysis of the sorption of crystal violet and methylene blue from aqueous solutions onto an agro-waste derived activated carbon. Appl. Water Sci. 10 (6), 1–11.
Joshi, S., Pokharel, B., 2013. Preparation and characterization of activated carbon from lapsi (Choerospondias axillaris) seed stone by chemical activation with potassium hydroxide. J. Inst. Eng. 9 (1), 79–88.
Juang, R., Yei, Y.L.C., Lin, K., Lu, H., Wang, S., Sun, A., 2018. Synthesis of magnetic Fe3O4/activated carbon nanocomposites with high surface area as recoverable adsorbents. J. Taiwan Inst. Chem. Eng. 90, 51–60.
Kakhki, R., Mohammadpoor, M., Faridi, R., Bahadori, M., 2020. The development of an artificial neural network–genetic algorithm model (ANN-GA) for the adsorption and photocatalysis of methylene blue on a novel sulfur–nitrogen co-doped Fe2O3 nanostructure surface. RSC Adv. 10 (10), 5951–5960.
Kangmennaa, A., Acquah, S., Forkuo, R., Adusei, J., Atongo, G., Amarh, F., Opoku, F., Agorku, E., 2024. Methylene blue dye adsorption on Ghana's activated clay from Teleku Bukazo. J. Dispersion Sci. Technol. 1–14.
Karthik, C., Suresh, S., Mirulalini, S., Kavitha, S., 2020. A FTIR approach of green synthesized silver nanoparticles by Ocimum sanctum and Ocimum gratissimum on mung bean seeds. Inorganic and Nano-Metal Chemistry 50 (8), 606–612.
KAYA, N., ERDEM, F., 2023. Artificial neural network approach for lead removal from aqueous solution by agricultural waste derived biochars. Sigma 41 (1), 80–89.
Keppetipola, N., Dissanayake, M., Dissanayake, P., Karunarathne, B., Dourges, M., Talaga, D., Servant, L., Olivier, C., Toupance, T., Uchida, S., Tennakone, K., 2021. Graphite-type activated carbon from coconut shell: a natural source for eco-friendly non-volatile storage devices. RSC Adv. 11 (5), 2854–2865.
Khan, T., Mustafa, M., Isa, M., Manan, T., Ho, Y., Lim, J., Yusof, N., 2017. Artificial neural network (ANN) for modelling adsorption of lead (Pb (II)) from aqueous solution. Water, Air, Soil Pollut. 228, 1–15.
Kheddo, A., Rhyman, L., Elzagheid, M., Jeetah, P., Ramasami, P., 2020. Adsorption of synthetic dyed wastewater using activated carbon from rice husk. SN Appl. Sci. 2 (12), 1–14.
Kristianto, H., Arie, A., Susanti, R., Halim, M., Lee, J., 2016. The effect of activated carbon support surface modification on characteristics of carbon nanospheres prepared by deposition precipitation of Fe-catalyst. In: IOP Conference Series: Materials Science and Engineering.
Kuang, Y., Zhang, X., Zhou, S., 2020. Adsorption of methylene blue in water onto activated carbon by surfactant modification. Water 12 (2), 587.
Kumari, S., Rajput, V., Minkina, T., Rajput, P., Sharma, P., Verma, A., Agarwal, S., Garg, M., 2022. Application of RSM for bioremoval of methylene blue dye from industrial wastewater onto sustainable Walnut shell (Juglans regia) biomass. Water 14 (22), 3651.
Kurniawati, D., Sari, T., Adella, F., Sy, S., 2021. Effect of contact time adsorption of rhodamine B, methyl orange and methylene blue colours on Langsat shell with batch methods. J. Phys. Conf. 1788 (1), 012008.
Kusuma, H., Aigbe, U., Ukhurebor, K., Onyancha, R., Okundaye, B., Simbi, I., Ama, O., Darmokoesoemo, H., Widyaningrum, B., Osibote, O., Balogun, V., 2023. Biosorption of Methylene blue using clove leaves waste modified with sodium hydroxide. Results in Chemistry 5, 100778.
Lee, X., Hiew, B., Lai, K., Tee, W., Thangalazhy-Gopakumar, S., Gan, S., Lee, L., 2021. Applicability of a novel and highly effective adsorbent derived from industrial palm oil mill sludge for copper sequestration: central composite design optimisation and adsorption performance evaluation. J. Environ. Chem. Eng. 9 (5), 105968.
Li, H., Liu, L., Cui, J., Cui, J., Wang, F., Zhang, F., 2020. High-efficiency adsorption and regeneration of methylene blue and aniline onto activated carbon from waste edible fungus residue and its possible mechanism. RSC Adv. 10 (24), 14262–14273.
Lopes, K., de Oliveira, H., Serpa, J., Torres, J., Nogueira, F., de Freitas, V., Borges, K., Silva, M., 2021. Nanomagnets based on activated carbon/magnetite nanocomposite for determination of endocrine disruptors in environmental water samples. Microchem. J. 168, 106366.
Makhado, E., Motshabi, B., Allouss, D., Ramohlola, K., Modibane, K., Hato, M., Jugade, R., Shaik, F., Pandey, S., 2022. Development of a ghatti gum/poly (acrylic acid)/TiO2 hydrogel nanocomposite for malachite green adsorption from aqueous media: statistical optimization using response surface methodology. Chemosphere 306, 135524.
Makomere, R., Rutto, H., Koech, L., Banza, M., 2023. The use of artificial neural network (ANN) in dry flue gas desulphurization modelling: Levenberg–Marquardt (LM) and Bayesian regularization (BR) algorithm comparison. Can. J. Chem. Eng. 101 (6), 3273–3286.
Martis, L., Parushuram, N., Sangappa, Y., 2022. Preparation, characterization, and methylene blue dye adsorption study of silk fibroin–graphene oxide nanocomposites. Environ. Sci. J. Integr. Environ. Res.: Advances 1, 285–296.
Mfon, R., Hall, S., Sarua, A., 2020. Effect of Ocimum gratissimum plant leaf extract concentration and annealing temperature on the structure and optical properties of synthesized zinc oxide nanoparticles. EDUCATUM Journal of Science, Mathematics and Technology 7 (1), 1–13.
Miyah, Y., Lahrichi, A., Idrissi, M., Khalil, A., Zerrouq, F., 2018. Adsorption of methylene blue dye from aqueous solutions onto walnut shells powder: equilibrium and kinetic studies. Surface. Interfac. 11, 74–81.
Mohammadi, H., Nekobahr, E., Akhtari, J., Saeedi, M., Akbari, J., Fathi, F., 2021. Synthesis and characterization of magnetite nanoparticles by co-precipitation method coated with biocompatible compounds and evaluation of in-vitro cytotoxicity. Toxicol Rep 8, 331–336.
Moosavi, S., Lai, C., Gan, S., Zamiri, G., Akbarzadeh Pivehzhani, O., Johan, M., 2020. Application of efficient magnetic particles and activated carbon for dye removal from wastewater. ACS Omega 5 (33), 20684–20697.
Moradi, M., Fazlzadehdavil, M., Pirsaheb, M., Mansouri, Y., Khosravi, T., Sharafi, K., 2016. Response surface methodology (RSM) and its application for optimization of ammonium ions removal from aqueous solutions by pumice as a natural and low cost adsorbent. Arch. Environ. Protect. 42 (2), 33–43.
Narendra Kumar, H., Chandra Mohana, N., Nuthan, B., Ramesha, K., Rakshith, D., Geetha, N., Satish, S., 2019. Phyto-mediated synthesis of zinc oxide nanoparticles using aqueous plant extract of Ocimum americanum and evaluation of its bioactivity. SN Appl. Sci. 1, 1–9.
Natrayan, L., Rajalakshmi, R., Amandeep Singh, K., Patil, P., Veeman, D., Paramasivam, P., 2022. Synthesis and optimization of Cr (VI) removal from aqueous solution by activated carbon with magnetic Fe3O4Nanoparticles by response surface methodology. Adsorpt. Sci. Technol. 2022.
Natrayan, L., Niveditha, V., Nadh, V., Srinivas, C., Dhanraj, J., Saravanan, A., 2024. Application of response surface and artificial neural network optimization approaches for exploring methylene blue adsorption using luffa fiber treated with sodium chlorit. J. Water Proc. Eng. 58, 104778.
Nguyen, N., Nguyen, L., Nguyen, T., Nguyen, T., Nguyen, D., Tran, T., 2022. Formation, antimicrobial activity, and biomedical performance of plant-based nanoparticles: a review. Environ. Chem. Lett. 1–41.
Nistor, M., Muntean, S., Ianoș, R., Racoviceanu, R., Ianași, C., Cseh, L., 2021. Adsorption of anionic dyes from wastewater onto magnetic nanocomposite powders synthesized by combustion method. Appl. Sci. 11 (19), 9236.
Obayomi, K., Lau, S., Zahir, A., Meunier, L., Jianhua, Z., Dada, A., Rahman, M., 2022. Removing methylene blue from water: a study of sorption effectiveness onto nanoparticles-doped activated carbon. Chemosphere, 137533.
Ofomaja, A., Naidoo, E., Pholosi, A., 2020. Intraparticle diffusion of Cr (VI) through biomass and magnetite coated biomass: a comparative kinetic and diffusion study. S. Afr. J. Chem. Eng. 32 (1), 39–55.
Onu, C., Ohale, P., Ekwueme, B., Obiora-Okafo, I., Okey-Onyesolu, C., Onu, C., Ezema, C., Onu, O., 2022. Modeling, optimization, and adsorptive studies of bromocresol green dye removal using acid functionalized corn cob. Cleaner Chemical Engineering 4, 100067.
Onyebuchi, C., Kavaz, D., 2019. Chitosan and N, N, N-trimethyl chitosan nanoparticle encapsulation of Ocimum gratissimum essential oil: optimised synthesis, in vitro release and bioactivity. Int. J. Nanomed. 14, 7707.
Ouldmoumna, A., Reinert, L., Benderdouche, N., Bestani, B., Duclaux, L., 2013. Characterization and application of three novel biosorbents "Eucalyptus globulus, Cynara cardunculus, and Prunus cerasefera" to dye removal. Desalination Water Treat. 51 (16–18), 3527–3538.
Parajuli, K., Sah, A., Paudyal, H., 2020. Green synthesis of magnetite nanoparticles using aqueous leaves extracts of Azadirachta indica and its application for the removal of as (V) from water. Green Sustain. Chem. 10 (4), 117–132.
Pekdemir, M., Tanyol, M., Torğut, G., 2022. Preparation of ε-Caprolactone/Fe3O4 magnetic nanocomposite and its application to the Remazol Brilliant Violet 5R dye adsorption from wastewaters by using RSM. J. Polym. Environ. 30 (10), 4225–4237.
Potgieter, J., Pardesi, C., Pearson, S., 2021. A kinetic and thermodynamic investigation into the removal of methyl orange from wastewater utilizing fly ash in different process configurations. Environ. Geochem. Health 43 (7), 2539–2550.
Prabhahar, M., Gomathi, K., Venkatesh, R., Stalany, V., Vijayan, D., Sassykova, L., Sendilvelan, S., Priya, V., Jijina, G., Selvaraj, R., 2022. Isothermic and kinetic study on removal of methylene blue dye using Anisomeles malabarica silver nanoparticles:

an efficient adsorbent to purify dye-contaminated wastewater. Adsorpt. Sci. Technol. 2022.
Prabu, S., Umamaheswari, A., Rajakumar, S., Bhuvaneswari, P., Muthupetchi, S., 2017. Development and evaluation of gel incorporated with synthesized silver nanoparticle from Ocimum gratissimum for the treatment of acne vulgaris. Am. J. Adv. Drug Deliv. 5 (3), 107–117.
Prasad, A., 2016. Iron oxide nanoparticles synthesized by controlled bio-precipitation using leaf extract of Garlic Vine (Mansoa alliacea). Mater. Sci. Semicond. Process. 53, 79–83.
Prasad, R., Yadav, K., 2020. Use of response surface methodology and artificial neural network approach for methylene blue removal by adsorption onto water hyacinth. Water Conservation and Management 4 (2), 83–89.
Raj, K., Joy, P., 2015. Coconut shell based activated carbon–iron oxide magnetic nanocomposite for fast and efficient removal of oil spills. J. Environ. Chem. Eng. 3 (3), 2068–2075.
Raju, R., Sakuntala, P., Jaleeli, K., 2017. FT-IR spectroscopic analysis of Ocimum-Gratissmium leaves. Int. J. Emerg. Trends Eng. Res. 5, 131–133.
Ramutshatsha-Makhwedzha, D., Mavhungu, A., Moropeng, M., Mbaya, R., 2022. Activated carbon derived from waste orange and lemon peels for the adsorption of methyl orange and methylene blue dyes from wastewater. Heliyon 8 (8), e09930.
Ratnam, M., Murugesan, M., Komarabathina, S., Samraj, S., Abdulkadir, M., Kalifa, M., 2022. Methylene blue adsorption BY UV-treated graphene oxide nanoparticles (UV/n-GO): modeling and optimization using response surface methodology and artificial neural networks. Int. J. Chem. Eng. 2022.
Razali, S., Aziz, M., Edinur, H., Ishak, A., 2020. Adsorption of methylene blue onto iron oxide magnetic nanoparticles coated with sugarcane bagasse. IOP Conf. Ser. Earth Environ. Sci. 596 (1), 012052.
Richard, D., Daouda, A., Arnaud, M., Balike, M., Domga, W., Bosco, T., 2022. Optimization of methylene blue adsorption onto activated carbon from Bos Indicus Gudali Bones using a Box Behnken experimental design. Am. J. Chem. 12 (1), 1–9.
Rodrigues, S., Silva, M., Torres, J., Bianchi, M., 2020. Use of magnetic activated carbon in a solid phase extraction procedure for analysis of 2, 4-dichlorophenol in water samples. Water, Air, Soil Pollut. 231, 1–13.
Rosly, N., Abdullah, A., Ahmad Kamarudin, M., Ashari, S., Alang Ahmad, S., 2021. Adsorption of methylene blue dye by calix [6] arene-modified lead sulphide (Pbs): optimisation using response surface methodology. Int. J. Environ. Res. Publ. Health 18 (2), 397.
Rout, P., Bhunia, P., Dash, R., 2015. A mechanistic approach to evaluate the effectiveness of red soil as a natural adsorbent for phosphate removal from wastewater. Desalination Water Treat. 54 (2), 358–373.
Saafie, N., Samsudin, M., Sufian, S., Ramli, R., 2019. Enhancement of the activated carbon over methylene blue removal efficiency via alkali-acid treatment. AIP Conf. Proc. 2124 (1).
Sahoo, T., Prelot, B., 2020. Adsorption processes for the removal of contaminants from wastewater: the perspective role of nanomaterials and nanotechnology. In: Nanomaterials for the Detection and Removal of Wastewater Pollutants. Elsevier, pp. 161–222.
Salazar-Rabago, J., Leyva-Ramos, R., Rivera-Utrilla, J., Ocampo-Perez, R., Cerino-Cordova, F., 2017. Biosorption mechanism of Methylene Blue from aqueous solution onto White Pine (Pinus durangensis) sawdust: effect of operating conditions. Sustainable Environment Research 27 (1), 32–40.
Selvaraju, R., Sakuntala, P., Jaleeli, K., 2021. GC–MS and FTIR analysis of chemical compounds in Ocimum Gratissimum plant. Biophysics 66 (3), 401–408.
Seoane, R., Santaeufemia, S., Abalde, J., Torres, E., 2022. Efficient removal of methylene blue using living biomass of the Microalga Chlamydomonas moewusii: kinetics and equilibrium studies. Int. J. Environ. Res. Publ. Health 19 (5), 2653.
Sharma, K., Guleria, S., Razdan, V., 2020. Green synthesis of silver nanoparticles using Ocimum gratissimum leaf extract: characterization, antimicrobial activity and toxicity analysis. J. Plant Biochem. Biotechnol. 29 (2), 213–224.
Simbi, I., Aigbe, U., Oyekola, O., Osibote, O., 2022. Optimization of biodiesel produced from waste sunflower cooking oil over bi-functional catalyst. Results in Engineering 13, 100374.
Singh, N., Balomajumder, C., 2017. Equilibrium isotherm and kinetic studies for the simultaneous removal of phenol and cyanide by use of S. odorifera (MTCC 5700) immobilized on coconut shell activated carbon. Appl. Water Sci. 7 (6), 3241–3255.
Solomon, L., Daminabo, V., George, W., 2019. Biocorrosion inhibition efficiency of locally sourced plant extracts obtained from aloe vera (Barbadensis miller) and scent leaf (Ocimum gratissimum). J. Biotechnol. Biomater. 8 (289).
Sonal, S., Prakash, P., Mishra, B., Nayak, G., 2020. Synthesis, characterization and sorption studies of a zirconium (IV) impregnated highly functionalized mesoporous activated carbons. RSC Adv. 10 (23), 13783–13798.
Sudarni, D., Aigbe, U., Ukhurebor, K., Onyancha, R., Kusuma, H., Darmokoesoemo, H., Osibote, O., Balogun, V., Widyaningrum, B., 2021. Malachite green removal by activated potassium hydroxide clove leaf agrowaste biosorbent: characterization, kinetic, isotherm, and thermodynamic studies. Adsorpt. Sci. Technol. 2021, 1–15.
Sulaiman, N., Mohamad Amini, M., Danish, M., Sulaiman, O., Hashim, R., 2021. Kinetics, thermodynamics, and isotherms of methylene blue adsorption study onto cassava stem activated carbon. Water 13 (20), 2936.
Tcheka, C., Abia, D., Iyedjolbo, B., Akpomie, K., Harouna, M., Conradie, J., 2022. Biosorption of cadmium ions from aqueous solution onto alkaline-treated coconut shell powder: kinetics, isotherm, and thermodynamics studies. Biomass Conversion and Biorefinery 1–12.
Thabede, P., Shooto, N., Naidoo, E., 2020. Removal of methylene blue dye and lead ions from aqueous solution using activated carbon from black cumin seeds. S. Afr. J. Chem. Eng. 33 (1), 39–50.
Togue Kamga, F., 2019. Modeling adsorption mechanism of paraquat onto Ayous (Triplochiton scleroxylon) wood sawdust. Appl. Water Sci. 9 (1), 1–7.
Udunwa, D., Onukwuli, O., Omotioma, M., 2017. Corrosion control of aluminum alloy in HCl medium using extract of Ocimum gratissium as inhibitor. Der Pharma Chem. 9 (19), 48–59.
Vinayagam, R., Zhou, C., Pai, S., Varadavenkatesan, T., Narasimhan, M., Narayanasamy, S., Selvaraj, R., 2021. Structural characterization of green synthesized magnetic mesoporous Fe3O4NPs@ ME. Mater. Chem. Phys. 262, 124323.
Vinayagam, R., Pai, S., Murugesan, G., Varadavenkatesan, T., Narayanasamy, S., Selvaraj, R., 2022. Magnetic activated charcoal/Fe2O3 nanocomposite for the adsorptive removal of 2, 4-Dichlorophenoxyacetic acid (2, 4-D) from aqueous solutions: synthesis, characterization, optimization, kinetic and isotherm studies. Chemosphere 286, 131938.
Xia, Y., Yao, Q., Zhang, W., Zhang, Y., Zhao, M., 2019. Comparative adsorption of methylene blue by magnetic baker's yeast and EDTAD-modified magnetic baker's yeast: equilibrium and kinetic study. Arab. J. Chem. 12 (8), 2448–2456.
Yang, J., Shojaei, S., Shojaei, S., 2022. Removal of drug and dye from aqueous solutions by graphene oxide: adsorption studies and chemometrics methods. NPJ Clean Water 5 (1), 1–10.
Yildiz, S., 2018. Artificial neural network approach for modeling of Ni (II) adsorption from aqueous solution by peanut shell. Ecological Chemistry and Engineering S 25 (4), 581–604.
Zango, Z., Dennis, J., Aljameel, A., Usman, F., Ali, M., Abdulkadir, B., Algessair, S., Aldaghri, O., Ibnaouf, K., 2020. Effective removal of methylene blue from simulated wastewater using ZnO-chitosan nanocomposites: optimization, kinetics, and Isotherm studies. Molecules 27 (15), 4746.
Zenebe, A., Yimer, A., Kuzhunellil, S., Demissie, H., 2021. Green synthesis of magnetic nanocomposite by Cordia Africana (CA) leave extract for the treatment of methylene blue contaminated water. Chemical Engineering Journal Advances 8, 100193.
Zhao, X., Baharinikoo, L., Farahani, M., Mahdizadeh, B., Farizhandi, A., 2022. Experimental modelling studies on the removal of dyes and heavy metal ions using ZnFe2O4 nanoparticles. Sci. Rep. 12 (1), 1–15.
Zheng, X., Zheng, H., Zhao, R., Sun, Y., Sun, Q., Zhang, S., Liu, Y., 2018. Polymer-functionalized magnetic nanoparticles: synthesis, characterization, and methylene blue adsorption. Materials 11 (8), 1312.